Astron. Astrophys. 280, 295–312 (1993)

ASTRONOMY AND ASTROPHYSICS

Solar radiation pressure perturbations for Earth satellites

I. A complete theory including penumbra transitions

D. Vokrouhlický [1,4], **P. Farinella** [2,3], **and F. Mignard** [4]

[1] Astronomical Institute, Charles University, Švédská 8, 15000 Prague 5, Czech Republic
[2] Observatoire de la Côte d'Azur, Dept. Cassini, CNRS URA 1362 B.P. 229. F-06304 Nice Cedex 4, France
[3] Dipartimento di Matematica, Università di Pisa, Via Buonarroti 2, I-56127 Pisa, Italy
[4] Observatoire de la Côte d'Azur, Dept. CERGA, CNRS URA 1360 Av. N. Copernic, F-06130 Grasse, France

Received March 24, accepted June 16, 1993

Abstract. We have studied the perturbative effect of the force due to direct solar radiation pressure on the dynamics of artificial satellites in a more comprehensive way than has been done so far. We have included a general model for the atmospheric refraction and extinction and have computed the illumination of a satellite for any geometric arrangement between it, the Earth and the Sun. This allowed us to investigate in detail the transition between the full sunlight and the shadow. We have considered separately the influence of the atmospheric refraction (treated according to geometrical optics) and the various physical processes in the atmosphere (absorption and scattering), to conclude that in general the flux attenuation during penumbra is most easily interpreted as due to a compression of the solar disk when viewed from the satellite through the Earth's atmosphere. The eclipsing of the finite–size solar disk by the solid Earth plays a minor role, whereas the refraction in the Earth atmosphere's produces an extended tail in the radiation force. However, the magnitude and duration of this tail depends upon the atmospheric conditions over a limited region of the Earth's surface. Several consequences of the theory have been exemplified by computing the perturbing force during penumbra on LAGEOS and other satellites.

Key words: celestial mechanics – artificial satellites, space probes – atmospheric effects

1. Introduction and overview

There are two dominant non–gravitational perturbations acting on the orbit of artificial Earth satellites: the atmospheric drag and the direct solar radiation pressure (Milani et al. 1987). Their relative magnitude depends primarily upon the altitude of the satellite. Below 800 km the drag is larger than the radiation force, and *viceversa*. Thus for most satellites used in space geodesy, which have high orbits tracked with centimetric accuracy, modelling the radiation force is of the utmost importance.

The perturbative effects of solar radiation pressure on the orbits of artificial satellites attracted the attention of dynamicists at the very beginning of the space age, both in the West (e.g. Parkinson et al. 1960; Musen 1960; Musen et al. 1960; Shapiro & Jones 1960) and in the Soviet Union (e.g. Polyakhova 1963). Some of these early studies — as well as several later ones — did not take into consideration the possible occurrence of spacecraft eclipses during passages through the Earth's shadow, when of course the radiation pressure temporarily vanishes, and were rather aimed at investigating the perturbations affecting the eclipse–free orbital arcs.

However, the potential importance of eclipses was recognized soon, and it was pointed out that a quartic equation needs to be solved to determine the intersections of the trajectory of a satellite with the Earth's (assumedly cylindrical) shadow (Kozai 1961; Wyatt 1961). Kozai also concluded that as a result of direct solar radiation pressure, long–term perturbations in the semimajor axis average out over one orbital period, except when the satellite undergoes eclipses (in which case, long–term perturbations of the order of the orbital eccentricity arise). Although this property was not explicitly stated by Kozai it is clearly included in his derivation. This result drew considerable attention, because unmodelled changes in the semimajor axis corrupted the determinations of atmospheric density based on the analysis of drag–induced effects (Wyatt 1961; Zadunaisky et al. 1961). Subsequent studies by Slowey (1974) and Aksnes (1976) followed basically Kozai's approach, integrating the Gauss or Lagrange perturbation equations with a discontinuous step–like model for the penumbra transition. All of these investigations dealt with the perturbations undergone by a spherically symmetrical satellite, so that the force could be assumed to be constant (apart from the eclipses) and directed away from the Sun; generalizations to spheroidal (Moore 1979; Zerbini 1980; Brookes & Ryland 1982a,b) and more complex shapes (Anselmo et al. 1983) were developed later.

Send offprint requests to: D. Vokrouhlický (Prague address)

A step forward was made by Ferraz–Mello (1964, 1972), who introduced the continuous *shadow function*, taking the values 1 out of the geometric Earth's shadow and 0 in the shadow, with the transition represented through a truncated expansion in the form of a Tchebychev or Fourier series. This approach was followed by several other investigators (e.g. Lála & Sehnal 1969; Lála 1970; and in the Russian literature Vashkovyak 1976; Aksenov 1977). However, the efficiency of this trick proved to be limited for most practical applications, as acknowledged by the above–mentioned authors. This is due to the fact that the 'smooth' shadow function was just an artificial mathematical representation of the real transition from sunlight to darkness, whose behaviour is determined by physical processes, i.e. the attenuation of the solar flux through the atmosphere and its partial interception by the solid Earth.

Indeed, only a few investigations were devoted to a detailed treatment of the penumbra transition dealing with its physical causes. The most remarkable work on this subject was carried out by Link in 1962. Although the formalism we are going to use is different, the basic physical ingredients of our theory are the same as analyzed by Link. He correctly pointed out that atmospheric processes (refraction, absorption, scattering) play a key role in shaping the real penumbra transition, and also explicitly stated several fundamental properties of 'atmospheric optics' related to the penumbra effect (see Sect. 4). More recently Kabeláč (1988) has analyzed the same problem using a simplified model. We will demonstrate that although his approach accounts for the essential physical processes, he missed an important effect, i.e. the vertical compression of the solar disk as viewed from the satellite through the Earth's atmosphere. This phenomenon occurs during the phase preceding the 'true' geometrical penumbra, characterized by the partial eclipse of the solar disk by the solid Earth.

In this paper we present a complete theory of the direct solar radiation pressure, including a detailed physical model of the transition between full sunlight and full shadow. Although in our examples we will restrict ourselves to the case of a spherically symmetric satellite, the formulation of the theory is general enough to be easily generalized to a satellite of arbitrary shape and arbitrary distribution of surface optical properties. Also, we will generally speak of the *penumbra effect*, but our approach takes into account not only the eclipsing of the solar disk by the solid Earth, but also the influence of the Earth's atmosphere. Actually, our formulae apply to every phase of the satellite revolution, including as well the 'normal' situation when the solar disk is fully viewed through the empty space.

Let us note that so far the mathematical technique we are going to use has not been commonly applied in the theory of non–gravitational perturbations of satellite orbits (e.g. Milani et al. 1987). Nevertheless, it is widely used in the theory of the radiative transfer (e.g. Mihalas 1970). As the treatment of the penumbra phenomena given here requires a good understanding of this mathematical approach, we deem it appropriate to include a brief explanation of it, which is given in Sect. 2 (together with some examples). In Sect. 3 we deal with the solar radiation pressure perturbations out of the eclipse or penumbra phases, i.e. when the satellite is in full sunlight. Although in this case the main results are well known, we have decided to include this discussion for the following reasons: (i) our theory will thus cover the whole satellite's orbit for any geometrical configuration with respect to the Earth and the Sun; (ii) this simpler case is useful to better understand the working of our mathematical technique in the more complex treatment of the penumbra effect; (iii) Eqs. (19)–(20) in Sect. 3 represent a precise solution for the radiation pressure perturbations, including 'corrections' which were not applied in earlier treatments. Sect. 4 will be devoted to model the geometrical and physical effects of the atmosphere, in order to calculate the perturbing force acting all over the penumbra transition. In Sect. 5 we will apply our general theory to specific satellites, with a particular emphasis on the passive laser—tracked satellite LAGEOS.

The latter choice was motivated by the need to model all the weak non–gravitational effects which may contribute to the observed LAGEOS orbit residuals (see Smith & Dunn 1980; and Scharroo et al. 1991, for a recent study), and thus degrade the orbital prediction and determination carried out in the framework of geophysical and geodynamical studies. For the same reasons, Vokrouhlický et al. (1993a,b) have recently developed detailed models of the perturbations caused by radiation pressure associated to Earth–reflected sunlight — the so–called *albedo effect*. In analogy with Vokrouhlický et al. (1993a), in this paper we will present the general theory and derive the components of the perturbing force versus time over a single revolution of the satellite. In a forthcoming paper (Vokrouhlický et al. 1993c), we we will discuss the 'additional' long–term perturbations which arise in the LAGEOS case from a detailed physical treatment of the penumbra transition, when compared to the predictions of simpler geometrical models.

2. The mathematical approach

We start by introducing a few concepts and notations which are not commonplace in satellite geodesy, although their use is widespread in radiative transfer theory. The essential quantities to describe the macroscopic properties of a continuous radiation field are: (i) the *radiative intensity* I, (ii) the *photon rays*. The intensity $I(\boldsymbol{n})$ at a point O, defined in such a way that the amount of energy dE crossing per unit time the area dA (having normal $\boldsymbol{N}$) and coming from the direction $\boldsymbol{n}$ (within a solid angle $d\Omega$) is given by

$$dE = I(\boldsymbol{n})\,(\boldsymbol{n}\cdot\boldsymbol{N})\,dA\,d\Omega\ . \tag{1}$$

Hereinafter (with the exception of Sect. 4.2.2) we will skip the frequency dependence of I. As we will usually parametrize the local direction $\boldsymbol{n}$ by two spherical angles (θ,ϕ) attached to a local frame centered at a point O, we will also use the notation $I(\theta,\phi)$. Of course , this description pertains only to bodies whose characteristic size exceeds the wavelength of the radiation. It is worth noting that astrophysicists have adopted the term *intensity* or *specific intensity* for $I(\boldsymbol{n})$, instead of the better words *brightness* or *radiance* (usually with the symbol L), with

the risk of provoking some confusion with the *intensity* I classically defined in photometry as the power radiated in a given direction by a *whole* radiation source. Nevertheless, in this paper we stick to the terminology most common in astrophysics and space science, and denote the brightness by $I(\boldsymbol{n})$.

By specifying at a point O a direction $\boldsymbol{n}$, one identifies an optical ray. Thus, I can be seen as attached to rays, and following one ray in space we 'transport' the radiative intensity along the ray itself. Two fundamental questions arise: (i) which is the rule specifying the geometry of rays?; and (ii) how to transport I along any specified ray? We summarize the answers. Within geometrical optics (which we will use throughout this paper), the ray guiding rule is provided by Fermat's principle: given the refractive index $\kappa(\boldsymbol{r})$ of the medium where the light propagates, the rays are such as to extremize the integral $\int \kappa[\boldsymbol{r}(s)]\, ds$, where s is an arbitrary affine parameter given along the ray. Treating this problem with the techniques of functional analysis, one ends up with Euler's variational differential equations for the ray. Garfinkel's theory of the atmospheric refraction, which we will summarize and use in Sect. 4, essentially solves these equations [see Garfinkel 1967, Eqs. (2)–(3)].

As for the transport of the radiative intensity along a specified ray, one has to solve the *radiative transfer equation* (see e.g. Mihalas 1970). We will not discuss this equation here; suffice it to say that it provides the rule specifying how the radiative intensity changes from point to point along the ray. This is important in our case, because we know the radiative intensity *only* on the source surface [the solar disk; see Eq. (12)]. *A priori*, we do not know how the radiative field 'spread into space', only solving the radiative transfer equation we get to know it. The equation has the simple (but not trivial) solution $I = I_0 =$ constant along the rays which do not interact with the medium they cross. Also, it is worth pointing out that the exponentially damped solution $I = I_0 \exp(-\tau)$ [where τ is the optical thickness; see Eqs. (31) and (37)] is the formal solution of the radiative transfer equation. We will use this solution to transport the radiative intensity in the scattering and absorbing atmosphere (see Sect. 4.2).

Now, let us describe the general algorithm to be used for computing the radiative energy flows and also the radiative force, that is the specific purpose of our work. At every point in the space we can specify a local orthonormal frame. As mentioned above, spherical coordinates (θ, ϕ) in such a frame can be used to characterize separate rays. We define the *tensorial moments* of the radiative intensity $M_{\alpha_1\alpha_2\ldots\alpha_k}$ as (see Mihalas 1970)

$$M_{\alpha_1\alpha_2\ldots\alpha_k} = \int_{(\theta,\phi)} d(\cos\theta)d\phi\; n_{\alpha_1} n_{\alpha_2} \ldots n_{\alpha_k}\, I(\theta,\phi)\;, \qquad (2)$$

where α_i are indexes spanning the values $(1, 2, 3)$ referring to the axes of the reference frame, and $n_{\alpha_i}(\theta, \phi)$ are the components of the unit vector in the direction (θ, ϕ) [i.e., we have $\boldsymbol{n}^T(\theta,\phi) = (\sin\theta\cos\phi, \sin\theta\sin\phi, \cos\theta)$]. Some of these tensorial moments, those of low orders k, are of special interest.

Putting $k = 1$ in Eq. (2), we obtain a vectorial quantity. For convenience (and to remain consistent Mihalas 1970), we shall use the notation F_α (or simply $\boldsymbol{F}$) instead of M_α. Equation (2) has then the following form

$$\boldsymbol{F} = \int_{(\theta,\phi)} d(\cos\theta)d\phi\; \boldsymbol{n}(\theta,\phi)\, I(\theta,\phi)\;. \qquad (3)$$

where the integration is extended to every direction $\boldsymbol{n}$. Because of the connection with the scalar flux [see Eq. (5) below] and for lack of a more insightful term, we will call the first–order moment $\boldsymbol{F}$ *vectorial flux*. Physically $\boldsymbol{F}$ is proportional to the radiative linear momentum leaving an infinitesimal sphere centered at O. We recall that when the z–coordinate is chosen along the normal to a surface element, Eq. (3) can be rewritten in the more usual form

$$F_z = \int_{(\theta,\phi)} d(\cos\theta)d\phi\;\cos\theta\, I(\theta,\phi)\;. \qquad (4)$$

More in general, the net scalar flux crossing a unit surface with normal $\boldsymbol{N}$ can be expressed as

$$F_s = \boldsymbol{F}\cdot\boldsymbol{N} = \int_{(\theta,\phi)} d(\cos\theta)d\phi\;\left[\boldsymbol{n}(\theta,\phi)\cdot\boldsymbol{N}\right]\, I(\theta,\phi)\;, \qquad (5)$$

Note that the vector flux (3) is more intrinsic to the radiative field than the scalar flux (5), because it is defined without reference to a specific direction of the outward normal of the elementary area. An important question follows: is $\boldsymbol{F}$ somehow connected with *the force* $\boldsymbol{f}$ exerted by the radiative field on the chosen surface element? The answer is negative. In general, there is no direct relation between the flux vector and radiative force vector. However, the two vectors are proportional to each other in a particular case, that of a spherical satellite having quasi–isotropic optical properties — see Eq. (11) below, and also Milani et al. 1987, and Vokrouhlický et al. 1993a.

In the general case, the radiative force is related to a higher–order moment in the hierarchy (2), namely that with $k = 2$. This is a tensorial ('two-indexed') quantity, which may be called the *impulse tensor* of the radiative field

$$M_{ij} = \int_{(\theta,\phi)} d(\cos\theta)d\phi\; n_i(\theta,\phi) n_j(\theta,\phi)\, I(\theta,\phi)\;. \qquad (6)$$

This quantity is related to radiation pressure, since the force exerted on a unit area with surface normal $\boldsymbol{N}$ can be expressed as

$$f_i = \frac{1}{c} M_{ij}\, N^j\;, \qquad (7)$$

where c is the speed of light. Equivalently we have in vectorial form

$$\boldsymbol{f} = \frac{1}{c}\int_{(\theta,\phi)} d(\cos\theta)d\phi\;\left[\boldsymbol{n}(\theta,\phi)\cdot\boldsymbol{N}\right]\boldsymbol{n}(\theta,\phi)\, I(\theta,\phi)\;. \qquad (8)$$

Thus the component of the force along the direction specified by $\boldsymbol{N}$ becomes

$$f_N = \frac{1}{c}\int_{(\theta,\phi)} d(\cos\theta)d\phi\;\left[\boldsymbol{n}(\theta,\phi)\cdot\boldsymbol{N}\right]^2\, I(\theta,\phi)\;, \qquad (9)$$

more usually employed to express the radiation pressure as the second moment in $\cos\theta$ (taking again the z–axis along the normal $\boldsymbol{N}$).

The total radiative force acting on a satellite is given by

$$\boldsymbol{f}_{\rm tot} = \int_{\mathscr{S}} dS\, \boldsymbol{f}\ , \tag{10}$$

where $\mathscr{S}$ represents the satellite's surface, to be parametrized by system of two surface coordinates u and v, i.e., $dS = dS(u,v)$. The resulting double integration required by Eqs. (8) and (10) may become a difficult task for spacecraft of complex shape, due to mutual shadowing of different parts of the surface. However, in the particular case of a spherical satellite of radius $R_{\rm a}$ and mass m, having uniform enough surface optical properties and placed in a radiative field homogeneous over its size, Eq. (10) can be integrated analytically (Vokrouhlický et al. 1993a), yielding for the perturbing acceleration $\boldsymbol{a}$ the final result

$$\boldsymbol{a} = \frac{\pi R_{\rm a}^2}{mc}\,\mathscr{C}_{\rm R}\boldsymbol{F}\ . \tag{11}$$

Here $\mathscr{C}_{\rm R}$ is a dimensionless coefficient of order unity, depending on the shape and the optical properties of the satellite's surface. Therefore, in this case the problem of calculating the radiative force is reduced to the evaluation of the radiative flux, as all the other quantities appearing in Eq. (11) are usually known from the satellite design and pre–launch tests. We stress that the acceleration is related to the vector flux in such a simple way only because of the spherical symmetry. Otherwise, the integration over the body surface does not yield a proportionality between the acceleration vector and the vector flux. Although in the applications to be discussed in Sect. 5 we will restrict ourselves to the case of spherically symmetrical satellites [hence we will use Eq. (11)], the formulation of our theory is more general, and it can be applied to spacecraft of arbitrary shape and optical properties. In that case, one has just to use more complicated formulae to calculate the radiative force, provided the radiative intensity $I(\boldsymbol{n})$ at the satellite's location is known (Vokrouhlický et al. 1993a).

From the previous discussion, it follows that the boundary conditions to calculate the radiative intensity field in the whole space have to be given at the radiative sources — in our case, the solar photosphere. We shall model the Sun as an extended source of radiation, whose brightness $I_\odot(\boldsymbol{n})$ at the solar surface depends only on the angle of emission with respect to the surface normal (whose cosine will be called μ). This property is at the origin of the limb darkening effect of the solar disk. We have

$$I_\odot(\mu) = F_\odot\ \Psi_\odot(\mu)\ , \tag{12}$$

where $F_\odot$ is the astrophysical flux emerging from the Solar photosphere, with the same dimensions as the intensity (J m^{-2} s^{-1}), and the function $\Psi_\odot(\mu)$ accounts for limb darkening. For our needs, a good approximation is provided by Eddington's solution for the radiative transfer in a grey atmosphere, leading to the following formula (Mihalas 1970):

$$\Psi_\odot(\mu) = \frac{3}{4}\left[\frac{7}{12} + \frac{1}{2}\mu + \mu\left(\frac{1}{3}+\frac{1}{2}\mu\right)\ln\left(\frac{1+\mu}{\mu}\right)\right]\ . \tag{13}$$

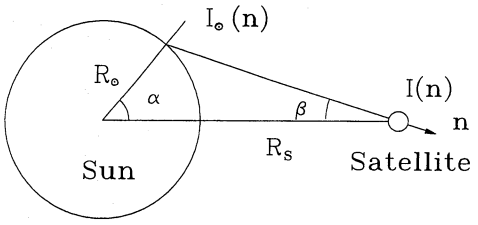

Fig. 1. Definition of the Sun–satellite geometry in the case full sunlight

Alternative, more complex formulae for $\Psi_\odot(\mu)$ (such as discussed in Mihalas 1970) could also be used instead of (13) for a more accurate treatment. In any case, our theory will be essentially devoted to the evaluation of the intensity at the satellite's location, knowing the function $I_\odot(\mu)$ at the surface of the Sun and the laws of light propagation.

The last topic to be specified is the choice of the reference frame at the satellite's position. Of course this choice is arbitrary, so it can be done in such a way to make easier the subsequent computations. We have chosen a *Sun–oriented local orthogonal frame* (x,y,z), whose axes are directed as follows: the z–axis is parallel to the satellite's geocentric radius vector, whereas the x–axis lies in the plane defined by the geocentric direction vectors of the satellite and the Sun, in such a way that its projection on the solar direction is antiparallel to it. The advantage of this choice is that the y–component of the radiative flux vector (hence of the perturbative force on a spherically symmetric satellite) does always vanish. Thus, we just need to calculate the other two components ($F_{\rm x}$ and $F_{\rm z}$).

Let us now summarize the successive steps of our general algorithm for obtaining the radiative force:

(1) At every point of space we introduce a local reference frame (in our case the Sun–oriented frame defined above), in which we compute the components of the quantities we are interested in (vector flux, satellite radiative acceleration).

(2) At every point of space the radiative field must be specified by the radiative intensity $I(\theta,\phi)$ for any (local) direction (θ,ϕ). Since *a priori* we know only the boundary conditions for I at the sources (in our case, at the solar photosphere), we solve for the optical rays from the source by applying Fermat's principle, and given these rays we solve the radiative transfer equation along them either in the empty space (in which case the radiative intensity is constant) or in a medium interacting with the radiation (the Earth's atmosphere, where Rayleigh scattering is assumed to occur).

(3) Then we have just to compute various moments of the radiative intensity with respect to the components of the local unit vector, according to Eq. (2). To obtain the radiative force acting on a unit area, the impulse tensor of the radiative field is generally needed, according to Eq. (6), and hence the total force acting on a satellite is obtained through the surface integral (10).

(4) In the particular case of a spherically symmetrical satellite, the calculation is more straightforward, since one does not need to compute all the 6 components of the impulse tensor $\mathbf{M}$ (the second–order moment of I), but only the 3 compo-

nents of the vector flux $\boldsymbol{F}$ (the first–order moment of I), since we can skip the integral (10) and use directly Eq. (11).

To illustrate the general procedure outlined above, we consider the simple case when $I_\odot(\mu) = I_0$ (implying that the Sun radiates like a Lambert source) and the (spherical) satellite is in full sunlight and absorbs all the incident light. If $R_\odot$ is the radius of the Sun and R_s the distance of the satellite from it, the radiative acceleration can be easily derived from the conservation of the solar energy output as

$$a = \frac{\pi R_a^2}{mc}(\pi I_0)\left(\frac{R_\odot}{R_s}\right)^2 , \tag{14}$$

where πI_0 is the radiant power of the Sun per unit surface. Alternatively, we can apply Eq. (11), whence we obtain for the non–zero component of the acceleration:

$$a = \frac{\pi R_a^2}{mc}\int I(\boldsymbol{n})\cos\beta d\Omega , \tag{15}$$

since it is easy to show that $\mathscr{C}_R = 1$ for a fully absorbing sphere. Here the intensity $I(\boldsymbol{n})$ at the satellite is given by $I(\boldsymbol{n}) = I_0$ for $\beta \in [0, \beta_{max}]$ (with $\sin\beta_{max} = R_\odot/R_s$; see Fig. 1), and $I(\boldsymbol{n}) = 0$ elsewhere, because in this simple case the light rays are straight lines and the radiative intensity has the constant value I_0 when transported along them. Thus the integral (15) reduces to

$$a = \frac{2\pi^2 R_a^2 I_0}{mc}\int_{(1-\frac{R_\odot^2}{R_s^2})^{1/2}}^{1}\cos\beta\, d(\cos\beta) = \frac{\pi^2 R_a^2 I_0}{mc}\left(\frac{R_\odot}{R_s}\right)^2 . \tag{16}$$

This coincides with Eq. (14), which was derived by a very different physical argument (energy conservation).

3. Radiation pressure perturbations in full sunlight

In this section we briefly derive the main equations related to the direct solar radiation pressure when the satellite is in full sunlight. In this case, we assume that the light rays are well represented by straight lines (which do extremize the Fermat integral for a medium with constant refractive index) and that the radiative intensity is conserved along the rays (corresponding to the solution of the radiative transfer equation for a non–absorbing medium). The only change with respect to the computation given at the end of Sect. 2 is that we are now going to use the more realistic Eqs. (12) and (13) for the solar limb darkening, instead of Lambert's law. We now describe the satellite's position through its geocentric position r and its geocentric angular distance from the Sun's centre ω.

The components of the vector flux can be computed by exploiting the advantages of the chosen local Sun–oriented reference frame, where the spherical coordinates (θ, ϕ) can be defined. The two non–vanishing components are

$$F_x = \int_{(\theta,\phi)} d(\cos\theta)d\phi\ \sin\theta\ \cos\phi\, I(\theta,\phi) ,$$
$$F_z = \int_{(\theta,\phi)} d(\cos\theta)d\phi\ \cos\theta\, I(\theta,\phi) . \tag{17}$$

Actually, in this particular case an even better choice of the local reference frame is available: if we take the z–axis along the heliocentric position vector of the satellite, the orientation of the other two axes being arbitrary, due to symmetry reasons the radiative intensity does not depend upon the ϕ angle (defined in the new frame), and as consequence the only non-vanishing component of the vector flux is

$$F_z = 2\pi F_\odot \int_{(\theta)} d(\cos\theta)\ \cos\theta\, \Psi_\odot[\mu(\theta)] , \tag{18}$$

where we have used Eq. (12), the θ angle is also defined in the new frame, and the limits of integration are the same as in Eq. (16). To proceed further, we would need to write down explicitly the function $\Psi_\odot[\mu(\theta)]$. In fact, it is better to change variables in such a way to switch the integration from 'over the local radiative field' to 'over the solar surface'. This will also allow us to compare our result with previously obtained formulae. The solar surface elements can be parametrized by the angle α (see Fig. 2). We do not write down here the simple relations used to transform θ into α, as they can be found in the appendix of Vokrouhlický & Sehnal (1993a). These authors define the function

$$\mathscr{J}(\rho_1) = \rho_1^2\int_{\rho_1}^{1} d\mu_\alpha(\mu_\alpha - \rho_1)(1 - \mu_\alpha\rho_1)$$
$$\zeta^{-2}(\mu_\alpha,\rho_1)\Psi_\odot[(\mu_\alpha - \rho_1)\zeta^{-1/2}(\mu_\alpha,\rho_1)] , \tag{19}$$
$$\zeta(\mu_\alpha,\rho_1) = 1 - 2\rho_1\mu_\alpha + \rho_1^2 ,$$

where $\rho_1 = \left(R_\odot/R\right)$ (R being Sun–Earth distance) and $\mu_\alpha = \cos\alpha$, the flux component (18) can be rewritten in the Sun–oriented reference frame as

$$F_x = 2\pi F_\odot \mathscr{J}\left[\rho_1\zeta^{-1/2}(\cos\omega,\rho_2)\right]\sin\theta_s ,$$
$$F_z = 2\pi F_\odot \mathscr{J}\left[\rho_1\zeta^{-1/2}(\cos\omega,\rho_2)\right]\cos\theta_s , \tag{20}$$

where

$$\theta_s = \arcsin\left\{\sin\omega\zeta^{-1/2}(\cos\omega,\rho_2)\right\} ,$$

with $\rho_2 = \left(r/R\right)$. Note that Eqs. (20) fully account for variations of the satellite–emitter distance, caused by the finite size of the Sun (through the factor ρ_1) and the satellite's geocentric motion (through ρ_2). A commonly used approximation in computing the solar radiation pressure is based on setting $\rho_1 = \rho_2 = 0$ in Eqs. (19)–(20), except for the ρ_1^2 factor standing before the integral in Eq. (19).

The radiative flux components can then be transformed in a straightforward way from the Sun–oriented local frame to a global, quasi–inertial geocentric frame (with the X–axis oriented towards the vernal equinox and the Z–axis parallel to the Earth's polar axis) and subsequently to the Gauss orbit–related frame (yielding Gauss' components S, T and W of the perturbative acceleration, see e.g. Brouwer & Clemence, 1961).

In the more general situations considered in the following we will transport the radiative intensity from the Sun to the satellite, taking into account the refraction and absorbtion in the

Earth's atmosphere. Because of the curvature of the rays in the atmosphere, we will need to find the points and the directions of emission of the light rays on the photosphere which eventually reach the satellite surface.

4. Penumbra phase perturbations

In this section we deal with the application of our general theory to compute the perturbing acceleration on a satellite moving gradually into the Earth's shadow, namely during the phase when at least part of the solar rays cross the atmosphere before reaching the satellite.

In order to calculate the effects of refraction, we assume that the Earth's atmosphere is as a spherical polytropic troposphere, according to Garfinkel's (1944, 1967) model. We neglect the contribution of the upper (roughly isothermal) atmospheric layers, as they contribute to the atmospheric refraction only by a few milliarcseconds (Garfinkel 1944). With this truncated model, the accuracy of the refraction theory is of about 5 milliarcseconds. We will not repeat here the intricate formulae given by Garfinkel, but just summarize the essential assumptions of his theory, as they equally apply to our current computations:

(1) The atmospheric density profile is spherically symmetric with respect to the centre of the Earth, and the planet is assumed to be spherical as well;
(2) the atmosphere behaves as an ideal gas, with a polytropic adiabatic function characterized by an index n;
(3) the refractive index of the air, κ, follows the Gladstone—Dale law.

Under these assumptions, Garfinkel showed that the decrease with altitude (h) of the refractive index can be expressed as

$$\kappa(h) = 1 + \alpha\left(1 - 2\gamma^2 \frac{h}{R_\oplus + h}\right)^n , \qquad (21)$$

where

$$2\gamma^2 = \frac{g_0 R_\oplus}{(n+1)\mathscr{R}T_0} .$$

Here α is a model parameter giving the refractive index at the surface ($h = 0$), g_0 is Earth's surface gravity acceleration, $\mathscr{R}$ is the air gas constant ($\approx 287\,\mathrm{J\,kg^{-1}K^{-1}}$), $R_\oplus$ is the Earth's radius, T_0 is the temperature at the bottom of the atmosphere and n is the polytropic index, derived from the atmosphere bottom conditions (the temperature gradient T_0'). Note that $\mathscr{R}T_0/g_0 \approx 8$ km is the scale height of an isothermal atmosphere. In the polytropic model, the top of the atmosphere is specified by $\kappa(h_\mathrm{T}) = 1$, yielding an altitude $h_\mathrm{T} = R_\oplus(2\gamma^2 - 1)^{-1} \approx (n+1)\mathscr{R}T_0/g_0$ of the order of 50 km (see McCartney 1976).

The essential input parameters required by Garfinkel's atmospheric refraction model are the *temperature* T_0, the *temperature gradient* T_0' and the *pressure* p_0 at the Earth's surface, and in addition a *humidity factor*, i.e. the water vapor pressure p' in the air. From this information, we aim at calculating the magnitude of the refraction angle $\mathrm{Re}(h)$ for an atmosphere–crossing ray reaching the minimum (*grazing*) altitude h. At the grazing point, the apparent zenith angle of the light source is by definition 90°.

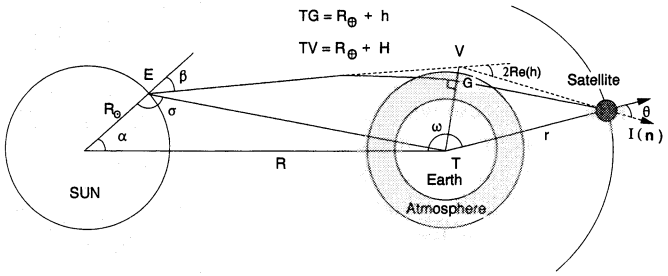

Fig. 2. Illustration of the bending of a light ray in the Earth's atmosphere and the associated geometrical parameters used in the text

In our approach, the Earth's atmosphere represents a medium whose influence on the radiative flux reaching the satellite (and hence on its perturbing acceleration) is twofold: (i) the differential refractive bending of solar rays results in a deformation of the solar image as seen from the satellite (this is a *geometrical*, lens–type phenomenon, to be treated in subsection 4.1); and (ii) absorption and scattering processes attenuate the radiative intensity of each solar ray crossing the atmosphere (we will model these *physical* processes in subsection 4.2). As the different solar rays forming the radiative field in the satellite's local frame are characterized by different paths in the atmosphere, it is necessary to follow each ray separately, and only at the end to build up the satellite–seen solar image. Thus, when evaluating the radiative flux acting on the satellite, we have to go back to its general expression. Calling $I[\mu(\theta,\phi);\tau]$ the intensity of a solar ray specified by a direction (θ,ϕ) in the local satellite frame, our starting formula (3) reads

$$\mathbf{F} = \int_{(\theta,\phi)} d(\cos\theta)d\phi\; \boldsymbol{n}(\theta,\phi)\, I[\mu(\theta,\phi);\tau] , \qquad (22)$$

where $\boldsymbol{n}(\theta,\phi)$ is a unit vector specifying the direction (i.e., $\boldsymbol{n}^T(\theta,\phi) = (\sin\theta\cos\phi, \sin\theta\sin\phi, \cos\theta)$ and the two arguments in the intensity $I[\mu(\theta,\phi);\tau]$ stay for the two different effects mentioned above:

(1) $\mu(\theta,\phi)$ denotes the cosine of the angle between the starting ray and the normal to the solar surface, and it depends upon the bending of light rays in the atmosphere, hence corresponds to a purely geometrical effect;
(2) τ denotes half of the optical thickness of the atmosphere along the chosen ray (θ,ϕ), hence it is determined by physical processes.

Note that we do not know the value of intensity $I[\mu(\theta,\phi);\tau]$ *a priori*, but we have to solve for it. This requires to trace the chosen ray (θ,ϕ) back to the solar surface emitter, whose emissivity is characterized by the limb–darkening law [such as Eqs. (12)–(13)].

An essential feature of our approach is the possibility of separating the two types of effects contributing to the intensity in Eq. (22). In other words, we will always speak about a definite path of the chosen ray, specified by geometrical optics, and then estimate the physical effects of the atmosphere [item (2) above]

on this fixed ray. Thus, we do not include a full treatment of the light scattering processes in the atmosphere, but account for the atmospheric sunlight attenuation only through the optical thickness τ associated with each ray. We will describe some suitable approximations for estimating the τ–damping of the radiative intensity in subsection 4.2. On the other hand, in subsection 4.1 we are going to treat the geometrical effects [item (1) above] in full detail.

4.1. Geometrical effects

We consider now the refractive bending of a ray connecting a point of the photosphere and the satellite and passing through the atmosphere of the Earth. As a first step, let us restrict the investigation to rays lying in the plane containing the Sun and the satellite. Later on, we will show how the results can be applied to light rays not lying in this plane.

The main parameters we are going to use are illustrated in Fig. 2 and have the following meaning: the basic lengths are the geocentric distance of the Sun R, the geocentric distance of the satellite r, the Earth's radius $R_\oplus$, the solar radius $R_\odot$, the altitude h of the atmospheric layer grazed by the ray under consideration, and the altitude H of the vertex V; the basic angles are the spherical angle θ, characterizing the ray in satellite's local frame, the Sun–satellite angular distance ω, the heliocentric position α of the source of radiation E on the photosphere, where the ray starts at an angle β from the normal, the angle σ between the directions of Sun's and the Earth's centers viewed from E, and the atmospheric refraction angle $\mathrm{Re}(h)$ of the ray reaching the grazing point G at the altitude h. We also recall the definitions

$$\rho_1 = \frac{R_\odot}{R} \quad , \quad \rho_2 = \frac{r}{R} \; . \tag{23}$$

It is well known that for the propagation of light in a spherically symmetrical atmosphere a first integral derived can be derived from the Snell law [see Garfinkel 1967, Eq. (2)]:

$$\kappa r \sin\psi = \text{constant} \; ,$$

where κ is the refractive index, r the distance from the Earth's centre and ψ the angle between the ray and the radius vector. From the sine theorem in a triangle we obtain for the factor Ψ defined as

$$\Psi(h) \equiv (R_\oplus + H)\cos \mathrm{Re}(h) = (R_\oplus + h)\kappa(h) \; . \tag{24}$$

By a repeated application of trigonometric relationships in the triangles shown in Fig. 2 we arrive at

$$\rho_1 \sin\sigma = \sin(\sigma + \alpha) \; , \tag{25a}$$

$$\rho_2 \sin\theta \, \sin\sigma = \eta_1 \sin\alpha \sin\big(\sigma + \eta_2\beta\big) \; , \tag{25b}$$

$$\beta = \eta_2\big(\alpha - \eta_1\xi\big) \; , \tag{25c}$$

where

$$\xi(\theta) = \pi + 2\mathrm{Re}[h(\theta)] - \omega - \theta \; ,$$

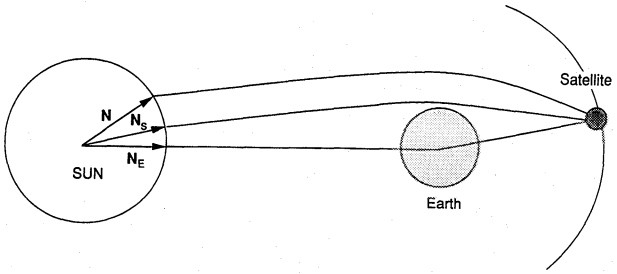

Fig. 3. The heliocentric vectors $\boldsymbol{N}_\mathrm{E}$ and $\boldsymbol{N}_\mathrm{S}$ and the emitter's heliocentric position $\boldsymbol{N}$, as defined in the text

and the altitude h of the grazing point as a function of θ is the solution of the equation

$$\Psi[h(\theta)] = r\sin\theta \; . \tag{26}$$

One can verify that in case of an atmosphere with a polytropically decreasing refraction index, as given by Eq. (21), Eq. (26) has a single solution, at least in the range of distance of interest in space geodesy.† This conclusion may become wrong when we move farther from the Earth, say at lunar distance for example. Of course, the previous equations apply also to the simpler case of rays avoiding the Earth's atmosphere. In this case κ = constant yields immediately $\mathrm{Re}(h) = 0$. This holds for all the equations to be obtained below.

The two quantities η_1 and η_2 are just required to adjust the signs, as we have taken positive values for all the angles appearing in Eqs. (25); they are derived as follows. Let $\boldsymbol{N}_\mathrm{E}$ be the unit vector along the Sun–Earth direction and $\boldsymbol{N}_\mathrm{S}$ a unit vector tangent to a ray reaching the satellite and emitted radially ($\beta = 0$) from the photosphere. Finally we define the unit vector $\boldsymbol{N}$ for an arbitrary ray as shown in Fig. 3. Then we have

$$\begin{aligned} &(\eta_1 = 1, \eta_2 = 1) && \text{if } \boldsymbol{N}_\mathrm{S} \text{ lies between } \boldsymbol{N}_\mathrm{E} \text{ and } \boldsymbol{N} \; , \\ &(\eta_1 = 1, \eta_2 = -1) && \text{if } \boldsymbol{N} \text{ lies between } \boldsymbol{N}_\mathrm{E} \text{ and } \boldsymbol{N}_\mathrm{S} \; , \\ &(\eta_1 = -1, \eta_2 = 1) && \text{if } \boldsymbol{N}_\mathrm{E} \text{ lies between } \boldsymbol{N}_\mathrm{S} \text{ and } \boldsymbol{N} \; . \end{aligned} \tag{27}$$

Starting from Eqs. (25)–(26), the basic problem is now that of finding the angle of emission from the photosphere of a grazing ray reaching the satellite at an angle θ with the radius vector. From Eq. (26) we can compute h from r and θ and then solve Eqs. (25) for α, β and σ. Unexpectedly, this can be worked out analytically and leads to

$$\alpha(\theta) = \eta_1\Big\{\xi(\theta) + \arcsin\big[\rho_1^{-1}(\rho_2\sin\theta - \sin\xi(\theta))\big]\Big\} \; , \tag{28a}$$

$$\sigma(\theta) = \arctan\Big\{\frac{\sin\alpha(\theta)}{\rho_1 - \cos\alpha(\theta)}\Big\} \; , \tag{28b}$$

$$\beta(\theta) = \eta_1\eta_2 \arcsin\big\{\rho_1^{-1}(\rho_2\sin\theta - \sin\xi(\theta))\big\} \; . \tag{28c}$$

In order to follow in time the transition from full sunlight to shadow we need also to solve Eqs. (25)–(26) for ω. Four

† Note, however, that this property is not trivial. Desert mirages provide a simple example of a special situation when this property is not satisfied (see e.g. Sampson 1993 for an intriguing 'solar mirage' phenomenon).

instants can be identified as defining the boundaries between different phases. The atmosphere starts playing a role when for the first time a ray emerging from the lowest part of the photosphere grazes the outermost layer of the atmosphere. At this point we have $\beta = \frac{\pi}{2}$, $\eta_1 = -\eta_2 = -1$ and $h = h_T$. An observer looking out of a window in the satellite would say that the solar disk just touches the atmosphere. We will call ω_{A1} the geocentric angular distance between the satellite and the Sun at this moment. Solving Eqs. (25)–(26) we obtain for this parameter

$$\omega_{A1} = \frac{\pi}{2} - \Lambda_+(\Psi_T; r, R_\odot, R) \,, \tag{29}$$

where $\Psi_T = \Psi(h_T)$ and

$$\Lambda_\pm(\Psi; r, R_\odot, R) = \arcsin\left\{ \frac{\Psi}{r}\left(\rho_1 \pm \frac{\Psi}{R}\right) \mp \sqrt{\left[1 - \left(\frac{\Psi}{r}\right)^2\right]\left[1 - \left(\rho_1 \pm \frac{\Psi}{R}\right)^2\right]} \right\} .$$

In a similar way, at the instant when the whole solar disk can be said to have penetrated the atmosphere, with the last solar ray grazing its outer boundary (in this case the same parameter values as above have to taken, but $\eta_1 = 1$), the value of ω is found to be

$$\omega_{A2} = \frac{3\pi}{2} - \Lambda_-(\Psi_T; r, R_\odot, R) \,. \tag{30}$$

It is worth remarking that the angular width of the atmospheric slab (having an approximate thickness of 50 km), when seen from a satellite such as LAGEOS, orbiting at an altitude of 5500 km, is about 16 arcmin, that is roughly half the apparent size of the *undistorted* solar disk. Thus one might erroneously conclude that the whole Solar disk cannot be seen through the atmosphere before eclipsing by the solid Earth starts. This would be true in absence of differential refraction of solar rays, which causes a strong distortion of the solar disk image, flattening it to such an extent that it can easily accommodate in the 16 arcmin width of the atmosphere. This has important consequences on the magnitude of the radiative force during the phase when only the atmosphere intercepts the sunlight directed to the satellite.

The apparent disappearance of the Sun behind the solid Earth (which would mark the entry into penumbra for an atmosphereless planet) starts when the first solar ray grazes the Earth's surface, namely when $\beta = \frac{\pi}{2}$, $\eta_1 = -\eta_2 = -1$ and $h = 0$. The corresponding value of ω is

$$\omega_P = \frac{\pi}{2} + 2\mathrm{Re}(0) - \Lambda_+(\Psi_0; r, R_\odot, R) \,, \tag{31}$$

where $\Psi_0 = \Psi(0)$. Finally, the entry into complete shadow corresponds to the total occultation of the Sun by the solid Earth, and occurs when the value of ω is

$$\omega_S = \frac{3\pi}{2} + 2\mathrm{Re}(0) - \Lambda_-(\Psi_0; r, R_\odot, R) \,. \tag{32}$$

It is remarkable that the angular distance covered by the satellite during this latter phase (defined as *phase III* below), that is $\omega_S - \omega_P$, is independent of the magnitude of the refraction angle 2Re(0), implying that the duration of time interval required for the solid Earth to eclipse the whole solar image is not affected by the atmospheric effects.

In summary, for a satellite like LAGEOS (or lower) we can recognize the following phases as it moves toward the Earth's shadow:

(1) $\omega < \omega_{A1}$: *phase 0* — the satellite is in full sunlight and the solar disk is neither deformed by the Earth atmosphere nor eclipsed by the solid Earth (this phase was dealt with in Sect. 3);
(2) $\omega_{A1} \le \omega < \omega_{A2}$: *phase I* — part of the Solar disk is viewed through the atmosphere;
(3) $\omega_{A2} \le \omega < \omega_P$: *phase II* — the whole Solar disk is viewed through the atmosphere;
(4) $\omega_P \le \omega < \omega_S$: *phase III* — part of the Solar disk is eclipsed by the solid Earth (we will call this the 'true penumbra' phase);
(5) $\omega_S \le \omega$: *phase IV* — the whole Solar disk is eclipsed by the Earth, and the satellite is in complete shadow.

These phases are illustrated in Fig. 4, which shows pictures of the solar disk, as it would be seen seen from LAGEOS during the penumbra transition (this Figure should be compared with Fig. 9 in Link 1962). It is apparent that the flattening of the solar disk is already significant during phase I, when the Sun plunges into the atmosphere. We will show in Sect. 5 that phases I and II determine the overall shape of the penumbra signal, while the contribution of phase III is limited to a 'tail effect'. We will also discuss the sensitivity of this perturbation tail to the absorption processes in the lower atmosphere.

Another possibility in dealing with Eqs. (25)–(26) is that of solving them for the maximum and minimum values of the angle θ in the local Sun–oriented frame, which correspond to the edges of the solar image in the 'vertical' direction. One again uses the conditions $\beta = \frac{\pi}{2}$ (as the searched rays graze the solar disk), $\eta_1 = \pm 1$ (with the plus and minus signs for the minimum and maximum values of θ, respectively) and $\eta_2 = 1$. Note, however, that now we miss the condition on the grazing height h, so that we have to solve for h. Manipulating Eqs. (25)–(26), we get

$$\frac{\Psi(h)}{r} = \zeta^{-1}\left(\cos\varpi(h), \rho_2\right)\left[\sin\varpi(h)\sqrt{\zeta\left(\cos\varpi(h), \rho_2\right) - \rho_1^2} + \eta_1\rho_1\left(\rho_2 - \cos\varpi(h)\right)\right] , \tag{33}$$

$$\varpi(h) = \omega - 2\mathrm{Re}(h) \,.$$

This equation can be solved numerically for h by an iterative technique. By means of Eq. (26), the maximal and minimal values of the θ angle for the Solar disk are found to be

$$\theta_{\pm1} = \arcsin\left(\frac{\Psi_{\pm1}}{r}\right) , \tag{34}$$

where the (±1) labels refers to the solutions for h of Eq. (33) with $\eta_1 = \pm1$. Thus, we obtain for the 'vertical' angular width of the solar disk

$$\Delta\theta = \arccos\left\{ \frac{\Psi_{+1}\Psi_{-1}}{r^2} + \sqrt{\left[1 - \left(\frac{\Psi_{+1}}{r}\right)^2\right]\left[1 - \left(\frac{\Psi_{-1}}{r}\right)^2\right]} \right\} . \tag{35}$$

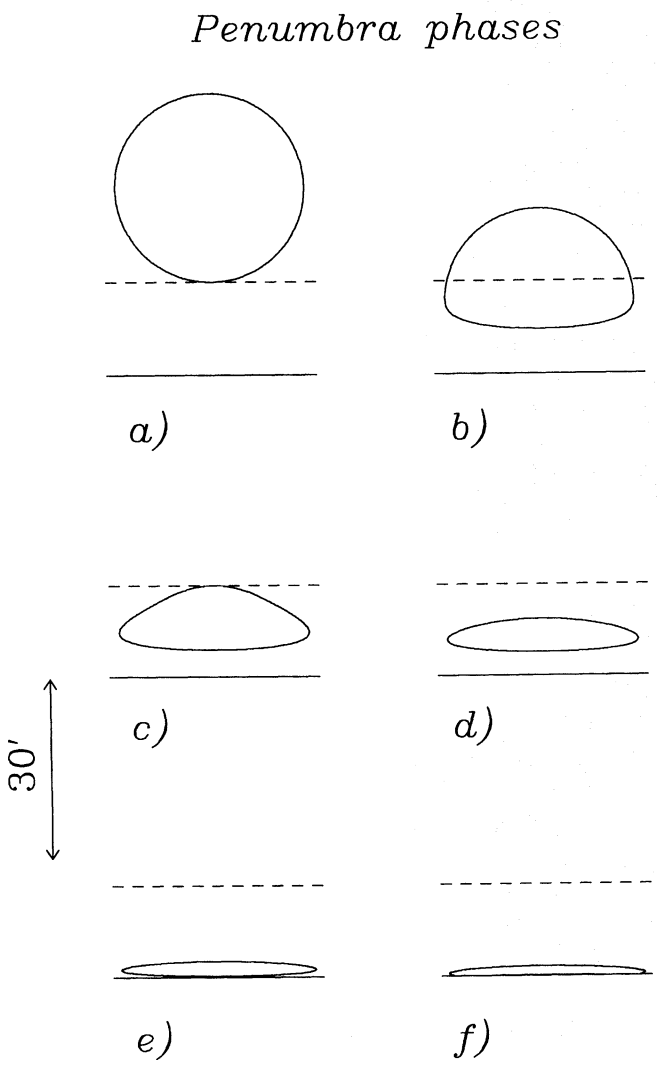

Fig. 4a–f. Different phases of the penumbra transition, as discussed in the text, correspond to varying shapes of the solar disk as seen from the LAGEOS satellite, owing to atmospheric refraction: **a** beginning of phase I, with partial penetration of the solar disk into the atmosphere; **b** phase I; **c**, **d**, **e** phase II, with the whole solar disk seen through the atmosphere; **f** *true penumbra* phase III, with part of the solar disk eclipsed by the Earth's solid body. The solid and dashed lines represent the Earth's horizon and the top of the atmosphere, respectively. The degree of vertical compression of the solar disk can be estimated comparing the solar images to the bars on the left, corresponding to 30 arcmin

Of course, these formulae apply during phases I and II, i.e., when $\omega \leq \omega_{\rm P}$ [note that in phase I Re = 0 in Eq. (33)]. As for phase III (true penumbra phase), the minimum θ angle of the visible solar disk corresponds to the Earth's horizon, so that $h_{+1} = 0$ formally holds in this case. The importance of the 'vertical compression' of the Solar disk even before reaching phase III, as predicted by Eq. (35), will be discussed in Sect. 5. Concerning Eq. (35), it can also be noted that, due to the monotonous decrease of the refractive index with height in Garfinkel's model atmosphere, no 'pathological' reversal of the solar image seen from the satellite is possible; as a consequence, $\Delta\theta$ is always positive, though it can reach fairly small values (see e.g. Fig. 6 below).

Having described in detail the geometry of rays lying in the Sun–satellite plane, we now turn to the problem of extending this solution to rays crossing this plane. It turns out that it is possible to keep the structure of the previously described solution and that just a *rescaling* of the solar radius, the Earth–Sun distance and the Sun–satellite angular distance is necessary.

Let us select a solar ray characterized by local spherical angles θ, ϕ in the Sun–oriented satellite frame, and call 'ϕ–slice' the plane defined by the geocentric satellite position vector and the vector tangent to the chosen ray. Whenever $\phi \neq 0$, the ϕ–slice differs from the Sun–satellite plane. We now consider the small circle defined by the intersection of the ϕ–slice with the solar sphere. By simple geometrical arguments it can be shown that the radius of this circle is $R_\odot(\phi) = R_\odot\left(1 - \rho_1^{-2}\sin^2\phi\sin^2\omega\right)^{1/2}$ (this can be taken as the 'ϕ–slice solar radius'), whereas the geocentric distance of the centre of this circle is $R(\phi) = R\left(1 - \sin^2\phi\sin^2\omega\right)^{1/2}$ (this can be taken as the 'ϕ–slice solar distance'). In the same manner, one shows that the angular distance of the Earth centered satellite radius vector and the centre of the small circle is given by $\cos\omega(\phi) = \cos\omega\left(1 - \rho_1^{-2}\sin^2\phi\sin^2\omega\right)^{-1/2}$. Also, we can introduce

$$\rho_1(\phi) = \frac{R_\odot(\phi)}{R(\phi)} \quad , \quad \rho_2(\phi) = \frac{r}{R(\phi)} \, ,$$

in analogy to ρ_1 and ρ_2. Note that the 'ϕ–width' of the solar disk follows simply from the previous formulae: $\phi_{\rm max} = \arcsin\left(\rho_1\sin^{-1}\omega\right)$.

The ray geometry problem has clearly the same structure in 'ϕ–slice' as in the Sun–satellite plane, provided the substitutions $\rho_1 \longrightarrow \rho_1(\phi)$ and $\rho_2 \longrightarrow \rho_2(\phi)$ are made. Thus, the fundamental equations read

$$\rho_1(\phi)\sin\sigma(\theta,\phi) = \sin[\sigma(\theta,\phi) + \alpha(\theta,\phi)] \, , \tag{36a}$$

$$\rho_2(\phi)\sin\theta\sin\sigma(\theta,\phi) = \eta_1\sin\alpha(\theta,\phi)\sin\left[\sigma(\theta,\phi) + \eta_2\beta(\theta,\phi)\right] \, , \tag{36b}$$

$$\beta(\theta,\phi) = \eta_2\left[\alpha(\theta,\phi) - \eta_1\xi(\theta,\phi)\right] \, , \tag{36c}$$

where

$$\xi(\theta,\phi) = \pi + 2{\rm Re}[h(\theta,\phi)] - \omega(\phi) - \theta$$

and $h(\theta,\phi)$ is determined implicitly by

$$\Psi[h(\theta,\phi)] = \rho_2(\phi)\sin\theta \, . \tag{37}$$

Therefore, all the solutions obtained when dealing with Eqs. (25)–(26) keep the same structure, provided the 'ϕ–slice quantities' are used. As for the deviation $\mu(\theta,\phi)$ of the ray's direction from the normal to the solar surface at the emitter point, simple geometry leads to

$$\mu(\theta,\phi) = \left[1 - \rho_1^{-2}\sin^2\phi\sin^2\omega\right]^{1/2}\cos\beta(\theta,\phi) \, , \tag{38}$$

which clearly generalizes the solution obtained for the rays lying in the Sun–satellite plane $\phi = 0$ [Eq. (28c)].

The formulae given in this Section represent a *full* treatment of the geometry of all solar rays crossing the atmosphere, in the frame of the atmospheric model described earlier. Our procedure to obtain the radiative flux [Eq. (22)] then consists in a detailed numerical integration, considering a large number of solar rays separately from each other.

4.2. Physical processes

We will now discuss the attenuation of the radiative intensity of a specified solar ray due to the physical processes in the atmosphere. We are not going to provide a full treatment of the atmospheric scattering of sunlight, as this represents a separate, very complicated problem without any simple analytical solution (see e.g. Chandrasekhar 1960, Van de Hulst 1980, or in a spherical atmosphere Sobolev 1975). As our goal is that of modelling radiation pressure perturbations of satellite orbits, we adopted a simplified, but still plausible approximation of the problem. Even with this simplification, one needs to address two issues related to the behaviour of the atmospheric absorption coefficient, namely: (i) its *altitude decrease*, and (ii) its *frequency dependence*. First, we will describe a simplified solution neglecting both effects; subsequently, we will introduce suitable correction factors to account for either of them.

In our simplest treatment of the atmospheric absorption problem we neglect any frequency dependence of the extinction processes. Under this assumption, one obtains

$$I\left[\mu\left(\theta,\phi\right);\tau\right] = I^{(0)}\left[\mu\left(\theta,\phi\right)\right]\exp(-2\tau)\,, \tag{39}$$

where $I^{(0)}[\mu(\theta,\phi)]$ is the radiative intensity before atmospheric attenuation (i.e., emitted by the corresponding solar surface element). The exponential damping comes from the formal solution of the equations of radiative transfer theory (Chandrasekhar 1960). We now need to determine the half–optical thickness τ in the atmosphere, which is given by

$$\tau = \int ds\;\chi(s)\,, \tag{40}$$

where the integral is extended over half the atmospheric path of the rays (here s denotes an arbitrary affine parameter along the solar ray in the atmosphere). A simple solution of Eq. (40) is obtained by assuming a constant absorption coefficient $\chi(h) = \chi^\star$ and neglecting the bending of rays in the atmosphere:

$$\tau^\star = \chi^\star\sqrt{(h_\mathrm{T}-h)(h_\mathrm{T}+h+2R_\oplus)}\,. \tag{41}$$

Were the atmosphere modelled as a sequence of layers with constant absorption coefficients, a sum of several terms such as (41) could be used. As for the value of $\chi^\star$, we have assumed that it is determined by Rayleigh scattering at the 'reference wavelength' $\lambda_\mathrm{r} = 550$ nm. This value is tabulated for normal atmospheric conditions and reads $\chi^\star = 1.162\times10^{-5}$ m^{-1} (McCartney 1976). In some models, we will also consider a stronger absorption in the bottom layer of the troposphere, simulating the effects of cloud coverage (see later).

Let us note that we have neglected several other mechanisms causing atmospheric absorption (water vapour, ozone, atmospheric dust grains etc.) in the current study. One can estimate the relative importance of these phenomena with respect to Rayleigh scattering using the table given in Sect. 55 of Allen (1976) (see also Table 2 in Kabeláč 1988). Actually, the results depend strongly on the instantaneous atmospheric conditions.

4.2.1. Correction for the altitude decrease of the absorption coefficient

Here, we derive a correction factor to the previous simple treatment of absorption, which accounts for the altitude decrease of the absorption coefficient χ in calculating the integral (40). We assume a pure Rayleigh scattering in the atmosphere, so that $\chi(s) = \chi^\star\left(\frac{\rho(s)}{\rho_0}\right)$, where $\rho(s)$ denotes the atmospheric density corresponding to a geometrical length s of the ray (measured from the perpendicular to the radius vector) and ρ_0 is the air density at the Earth's surface. Making the assumption of a polytropic atmosphere and neglecting the bending of rays, one obtains for the half–optical thickness [see Garfinkel 1967, Eq. (8)]:

$$\tau = \tau^\star\int_0^1 d\xi\left\{1-2\gamma^2\left[1-\left((\xi^2-1)\frac{\tau^{\star 2}}{R_\oplus^2\chi^{\star 2}}+\right.\right.\right.$$
$$\left.\left.\left.(1+\frac{h_\mathrm{T}}{R_\oplus})^2\right)^{-1/2}\right]^n\right\}\,, \tag{42}$$

If we consider the half–optical thickness given by Eq. (41) (and the corresponding exponential attenuation) as a 'reference solution' for the atmospheric absorption problem, the correction associated with a variable absorption coefficient can thus be expressed as a factor

$$f_\mathrm{alt}(\tau^\star) = \exp 2\left(\tau^\star-\tau\right) =$$
$$\exp\left\{2\tau^\star\left[1-\int_0^1 d\xi\left[1-2\gamma^2\left(1-\right.\right.\right.\right.$$
$$\left.\left.\left.\left.((\xi^2-1)\frac{\tau^{\star 2}}{R_\oplus^2\chi^{\star 2}}+(1+\frac{h_\mathrm{T}}{R_\oplus})^2)^{-1/2}\right)^n\right]\right]\right\}\,. \tag{43}$$

In Fig. 5a, we have plotted the the factor $f_\mathrm{alt}(\tau^\star)$ versus the reference optical thickness $\tau^\star$ for normal atmospheric conditions ($h_\mathrm{T} \doteq 48.34$ km, $2\gamma^2 \doteq 132.96$). From this figure, we can draw some interesting conclusions: (i) no significant correction needs to be made for small optical thickness, as here the ray penetrates just a small part of the atmosphere; (ii) the correction is sizeable for intermediate optical thickness, as the ray penetrates deeper in the atmosphere, but still grazes it at high altitudes, where the absorption coefficient is polytropically damped with respect to its value at the Earth's surface — in this case the simple solution (41) overestimates the atmospheric absorption; (iii) smaller corrections are needed for high optical thickness, as the corresponding ray grazes the Earth's surface and the role of the optically thin layers of the upper atmosphere is lower. In Sect. 5, we will discuss the way this correction affects the magnitude of the radiation pressure acceleration of LAGEOS during the penumbra passage.

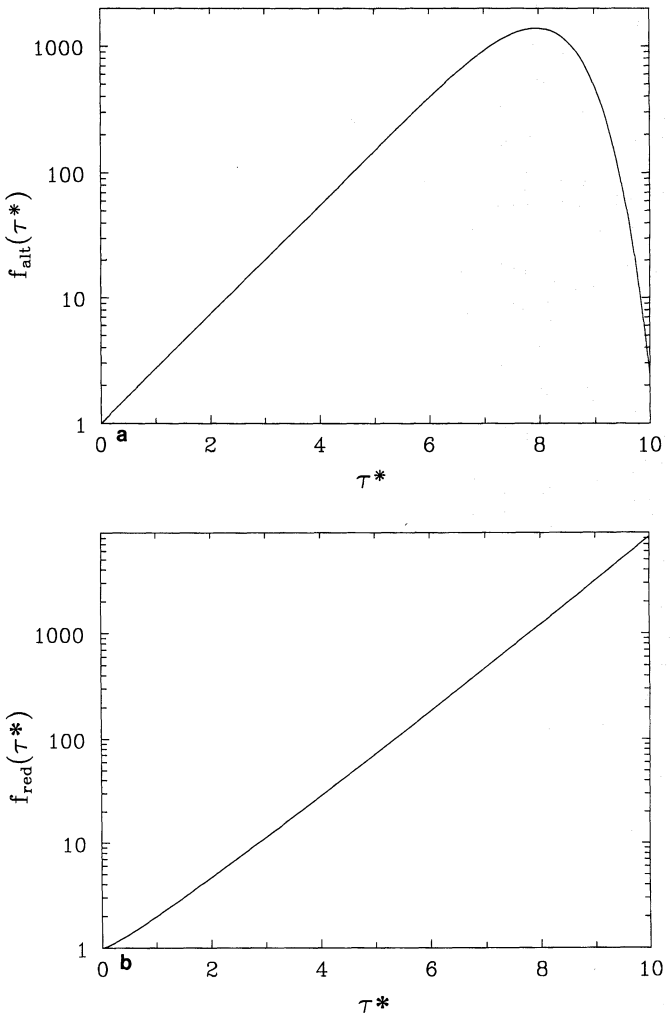

Fig. 5a and b. Correction factors accounting for realistic features of the atmospheric extinction: **a** f_{alt}, due to the altitude decrease of the absorption coefficient, vs. the reference optical thickness $\tau^\star$ given by Eq. (41); **b** f_{red}, due to frequency–selective absorption in a 'Rayleigh atmosphere', vs. $\tau^\star$ (see text).

4.2.2. Correction for frequency–selective absorption

Let us now discuss the possible importance of frequency–dependent scattering/absorption processes in the atmosphere, leading to the well known solar disk reddening effect near the horizon. In order to treat this effect, one has to consider the frequency distribution of the radiative intensity. We have assumed that the solar spectrum matches perfectly a black–body distribution with the effective temperature $T = 4560$ K (this corresponds to the bottom chromosphere temperature; see e.g. Allen 1976), i.e.:

$$I_\nu^{(0)} = B_\nu(T) = \frac{2h}{c^2} \frac{\nu^3}{\exp\left(\frac{h\nu}{kT}\right) - 1} , \tag{44}$$

where h is the Planck constant, c is the velocity of light, k is the Boltzmann constant and ν is the frequency (throughout this subsection the subscript ν indicates that the corresponding quantity depends upon frequency, a common notation in radiative transfer theory). The formal solution of the radiative transfer equations still assures that

$$I_\nu\left[\mu(\theta,\phi);\tau\right] = I_\nu^{(0)}\left[\mu(\theta,\phi)\right] \exp(-2\tau_\nu) , \tag{45}$$

where

$$\tau_\nu = \int ds\, \chi_\nu(s) . \tag{46}$$

In what follows, we assume a Rayleigh scattering in the atmosphere, i.e. $\chi_\nu = \chi_0 \nu^4$ (McCartney 1976). To obtain the frequency–integrated intensity in the satellite's local frame, we define an *absorption–averaged optical thickness* for a given ray as

$$2\bar{\tau} = -\ln\left\{ \frac{\int_0^\infty d\nu B_\nu(T) \exp\left(-2\tau_\nu\right)}{\int_0^\infty d\nu B_\nu(T)} \right\} . \tag{47}$$

Referring the absorption model to the previous simple approach based on a frequency–independent absorption coefficient, we obtain for each given ray a *solar–reddening correction factor* in the form

$$f_{red}(\tau^\star, \nu^4) = \exp 2(\tau^\star - \bar{\tau}) = \frac{15\exp(2\tau^\star)}{8\pi^4\beta\tau^\star} \int_0^1 \frac{d\xi}{\exp\left[\left(-\frac{1}{2\beta\tau^\star}\ln\xi\right)^{1/4}\right] - 1} \tag{48}$$

where the numerical constant β has the approximate value 9.233×10^{-4} and the argument ν^4 indicates the assumed Rayleigh–type dependence of the absorption coefficient upon frequency [in general, one might assume another form of τ_ν in Eq. (46)]. In the numerical calculations referring to this case, we will apply this correction factor to each solar ray constituting the radiative field in the satellite's local frame. It has to be remarked that the numerical evaluation of the integral (48) is rather delicate, as the integrand diverges when $\xi \to 0$; it can be proven, though, that the value of the integral converges. Several numerical methods treating successfully this type of integrals are available (e.g. Pérez-Jordá et al. 1992).

Figure 5b displays the $f_{red}(\tau^\star)$ versus $\tau^\star$ relationship. One can note a monotonic increase of this factor with the optical thickness $\tau^\star$. Values greater than 1 mean that there is such an amount of energy in the short–frequency part of spectrum, that the constant absorption factor adjusted to $\lambda = 550$ nm overestimates the attenuation in the simple model. Of course, the present results are also approximate, since the short–wavelength radiation is more efficiently absorbed in the atmosphere by other processes than Rayleigh scattering (Liou 1980). We will discuss the influence of the correction given by Eq. (48) on the radiation pressure penumbra perturbations in Sect. 5.

Let us point out that the joint effect of the two corrections treated in Sects. 4.2.1 and 4.2.2 is *not* equivalent to a simple product of the corresponding correction factors f_{alt} and f_{red}[‡].

‡ This fact already follows from the observation that often $f_{alt}(\tau^\star) f_{red}(\tau^\star) > \exp\tau^\star$, as it can be seen from Figs. 5a–b. Such a property would not be consistent with the attenuation of the radiative intensity due to extinction.

One could derive the joint effect of an altitude–dependent absorption coefficient *and* of a frequency–selective absorption by calculating

$$f_{\rm tot}(\tau^\star,\nu^4) = f_{\rm red}\left[\tau^\star,\nu^4 - \frac{1}{\tau^\star}\ln\left(f_{\rm alt}(\tau^\star\nu^4)\right)\right] . \qquad (49)$$

However, an analysis of this rather complicated correction factor is beyond the scopes of this paper.

Finally, note that our general formulation of the penumbra effect is not intrinsically linked to the treatment given in subsection 4.2 of the physical processes causing attenuation of light in the atmosphere. Instead of the simple assumptions leading to of our formulae (40), (43) and (48), we might have selected other relationships describing the altitude decrease and/or frequency dependence of the absorption coefficient, or even more sophisticated models for the optical thickness in the atmosphere, accounting for ray–bending phenomena (such as in Link & Neužil 1969 and Murray 1983).

5. Examples of the penumbra effect

As the main contribution of this paper is a detailed theory of the radiation pressure perturbations occurring when a satellite crosses the Earth's penumbra, we will focus our examples on this orbital phase. In particular, we intend to investigate the sensitivity of the way the perturbative acceleration decreases after entrance into the penumbra (or, equivalently, increases when exiting from the Earth's shadow) to changes of several physical parameters appearing in different parts of the theory (refraction theory, absorption model, etc.). We will be mainly concerned with LAGEOS, as for the orbital determination of this passive, nearly spherical, laser–tracked satellite an accurate treatment of the radiation pressure perturbations is essential (Milani et al. 1987; see also Sect. 1). We will discuss in a forthcoming paper (Vokrouhlický et al. 1993c) the possible long–term effects of the penumbra perturbations on LAGEOS' orbit. In this section, we will also give some examples for satellites orbiting at different altitudes than LAGEOS.

As regards the numerical treatment of the problem, we have adopted a short enough time step over LAGEOS' orbital motion (1 second, corresponding to 13,540 steps per revolution) that no important detail of the penumbra passage is lost because of a poor time resolution: actually, with this step the whole penumbra transition spans a few hundred steps. A dense enough integration grid is also necessary when the radiative flux integral (22) is calculated. We used 51 integration steps in both variables θ and ϕ. Note that the knowledge of the solar disk 'vertical edges' in terms of the local angle θ [provided by Eq. (34)] is important here, because in this way one can cover the whole solar image by an optimized grid: this significantly increases the accuracy of the result, or equivalently, keeping a given accuracy level, saves computing time. We have verified that using less than ≈ 50 grid centers when evaluating the integral (22) degrades the accuracy of the final results.

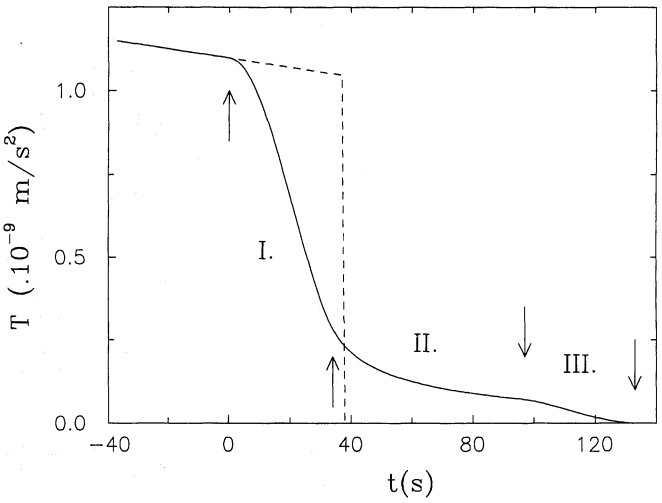

Fig. 6. The transverse acceleration component T due to solar radiation pressure on LAGEOS vs. time (in seconds) during the penumbra transition, modelled in different ways. The dashed curve represents the 'step approximation', the solid is derived from the present theory under the assumptions of no absorption and normal atmospheric conditions (see text). The interpretation of the various phases is discussed in the text

For our examples we have chosen the elements of LAGEOS' orbit corresponding to the epoch May 15, 1976, namely just after the launch of the satellite (see Table 1 in Barlier et al. 1986); the orientation of this orbit is such that it actually crosses the Earth's shadow and thus the satellite can undergo eclipses. For LAGEOS' area–to–mass ratio [appearing in Eq. (10)] we have adopted the same 7×10^{-3} cm^2 g^{-1} value used in Barlier et al. (1986), whereas for the $\mathscr{C}_{\rm R}$ coefficient we have adopted the value 1.13, in agreement with Rubincam & Weiss (1986). We are going to follow one revolution of the satellite, and focus on the behaviour of the T (transverse, in the orbital plane) component of the perturbing acceleration during the transition interval corresponding to the Earth shadow entry. The T component is important because it may give raise to semimajor axis changes leading to accumulating along–track orbital residuals; however, since in general the penumbra transition interval is much shorter than the orbital period, the orientation of the radiation force with respect to the satellite's motion changes very little during this interval, and thus the other two components would just be scaled by a nearly constant factor with respect to T.

Let us start by considering an absorption–free atmosphere, and adopting normal atmospheric conditions (see Garfinkel 1967): $p_0 = 760$ mm Hg, $T_0 = 273.15$ K, $T_0' = -0.005694$ K/m' (here m' represents the geopotential meter defined in Garfinkel 1967). In Fig. 6 we have plotted the decrease of T following LAGEOS' penumbra entry. The abscissa represents time in seconds measured since the beginning of the penumbra, i.e. the entry in phase I according to the terminology introduced in Sect. 3. For the sake of comparison, we have also plotted the curve corresponding to a 'step approximation', neglecting at all the penumbra effect (the step transition is assumed to occur when the line from the Sun's centre to the satellite becomes tangent to

the solid Earth's surface, assumed to be spherical); such an approximation is routinely used in the current orbit determination algorithms. We can easily recognize the different phases of the shadow penetration process, as listed in Sect. 3 and illustrated in Fig. 4. During phase I (with part of the solar disk plunged into the atmosphere) we observe a substantial decrease of T, which is just due to the compression of the atmospherically deformed part of the solar disk (see also Fig. 7). This compression effect continues also in phase II (when the whole solar disk is viewed from the satellite through the atmosphere), but the slope of the curve becomes smaller – here starts the *penumbra tail*. The true penumbra phase III (when the Earth begins to eclipse the solar disk) is characterized by a the slope getting greater again. This discontinuity in the derivative of the curve is due to the fact that the Earth's horizon represents now a *fixed* limit for the part of the solar disk visible from the satellite, while in the previous phases both limits of the solar disk (i.e., the corresponding θ angles in the local Sun–oriented reference frame) changed smoothly. All the examples we have analyzed support the conclusion, consistent with the interpretation of Fig. 6 given above, that the true penumbra phase (III) plays a minor role in determining the overall shape of the T decrease curve. Much more important is the influence of the atmospheric effects – refraction and absorption.

The durations of the various phases are: phase I: 34 s; phase II: 63 s; phase III: 34 s. Of course, these values depend on the assumed geometry of the passage, i.e., on the inclination of the apparent trajectory of the Sun with respect to the normal to the local horizon. This angle in our case is about 43°, owing to the fact that the orbit crosses the Earth's shadow in a fairly oblique way; when it approaches zero, the eclipse duration is maximum but the penumbra duration is minimum — some 84 s for LAGEOS. However, we have checked that apart from the duration factor, the qualitative features of the perturbation curves described above do not change with the orientation of the orbit and the Sun. It is worth noting that, first, the total duration of 131 s found with our theory is much longer than one would expect from a simple geometrical estimate. Secondly, and somewhat surprisingly (see the comment we made in Sect. 4.1), the interval when the whole disk is still visible, while penetrating through the atmosphere, corresponds to the longest part of the transition. The compression of the solar disk changes slowly, and this results into the formation of a characteristic tail. As we discussed in Sect. 3.1, the duration of the true penumbra phase is not increased by the refraction effects, and its value can be simply estimated by considering how long it takes to the Earth to eclipse the *undistorted* solar disk (see later).

We stress that the divergence of the solar rays penetrating the atmosphere is the dominant cause of the great atmospheric decrease of the radiation pressure in phase II (Fig. 6). From this point of view, as remarked by Link (1962), the Earth's atmosphere acts in the opposite way with respect to a converging lens (cf. in Fig. 4 of Link 1962). Another way to show the importance of the solar disk compression is by plotting the θ–extent of the solar disk in the local Sun–oriented frame, as given by Eq. (35). Figure 7 shows such a plot, where the different phases are identified as in the previous discussion about Fig. 6. Note

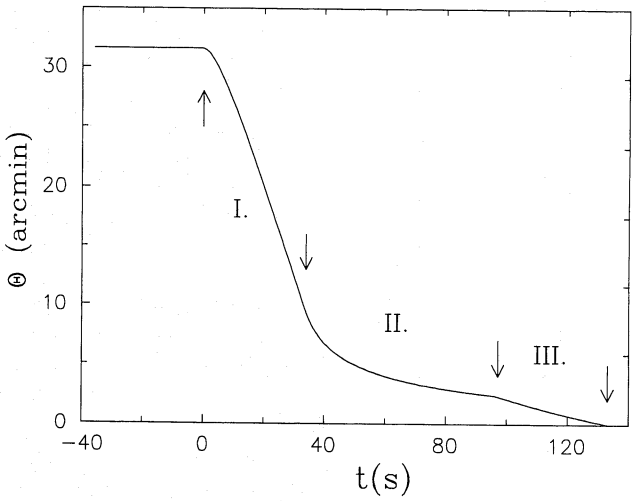

Fig. 7. The solar disk's 'θ–thickness' vs. time during the penumbra passage

that the minimum vertical thickness of the LAGEOS–seen solar disk, penetrating through the dense bottom layers of the atmosphere, is only 2.4 arcmin, more than one order of magnitude less than the 'undistorted' value (about 31 arcmin). Such an extreme compression is not at odds with the fact that the corresponding minimum vertical extent of the solar disk seen by an observer on the Earth's surface is about 24 arcmin (see e.g. McCartney 1976). Actually, there is an essential difference between the two cases. When the observer is on the Earth's surface, the two extreme solar rays limiting the vertical extent of the solar disk penetrate into the densest layers of the atmosphere. However, when the 'sunset' is seen from LAGEOS, one of the two limiting rays grazes the Earth's surface, whereas the other one crosses only fairly high layers of the atmosphere (reaching the minimum altitude of about 8.6 km for normal atmospheric conditions). Thus the latter ray is much less refracted, and as a result the oblateness of the LAGEOS–seen solar disk is amplified. This effect was also already discussed by Link (1962) (but essentially already in Link 1933).

In Fig. 8, still neglecting the atmospheric absorption processes, we compare the penumbra decrease of the T component for different assumptions about the state of the atmosphere. Curve 3 corresponds to conditions leading to a weaker atmospheric refraction, while the opposite holds for curve 1. The two curves cross each other because in phase I and at the beginning of phase II a higher radiation pressure arises when a weaker refraction results into a lower deformation of the solar disk; on the other hand, the 'tail' becomes longer under higher refraction conditions, due to a stronger ray bending. Thus the magnitude and the duration of the tail perturbation can change significantly as a response to variable atmospheric conditions; the difference between curves 1 and 3, when averaged over one full revolution, corresponds to an extra $< T >$ acceleration of a few times 10^{-13} m/s^2, just a factor 10 less than the unmodeled perturbations in LAGEOS' orbit.

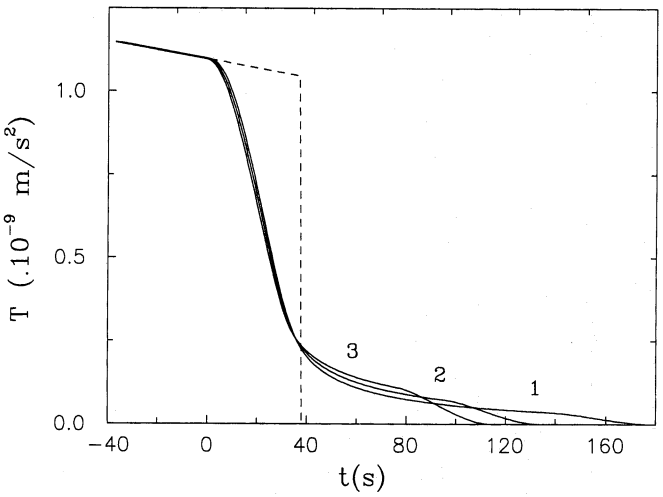

Fig. 8. The same as Fig. 6 but with different atmospheric conditions affecting refraction (no absorption is assumed to occur here): curve 1: p_0 = 730 mm Hg, T_0 = 253.15 K, T_0' = −0.004894 K/m'; curve 2: p_0 = 760 mm Hg, T_0 = 273.15 K, T_0' = −0.005694 K/m' (normal conditions); curve 3: p_0 = 790 mm Hg, T_0 = 293.15 K, T_0' = −0.006494 K/m'. We have used a humidity factor p_0' = 0 mm Hg in all cases

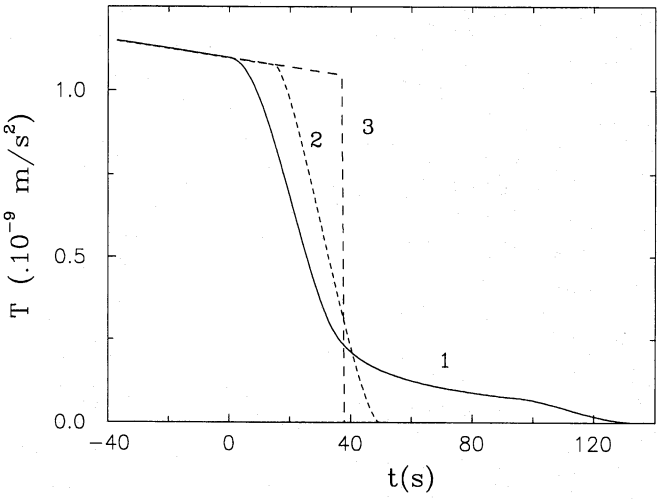

Fig. 9. The same as Fig. 6, but comparing the curve derived from our theory (curve 3) with those derived from simpler penumbra models: curve 1, the 'step approximation', and curve 2, with the solar flux attenuated in proportion to the visible portion of the solar disk eclipsed by an atmosphereless Earth (see text)

In order to compare the results of our theory, fully accounting for atmospheric refraction, with those of a simpler model neglecting refraction, one can consider the attenuation of the Solar flux from a hypothetical atmosphereless Earth, due to the gradual geometrical eclipsing of the finite–size solar disk by the horizon. The attenuation factor reads in this case

$$\mathscr{P} = \frac{1}{\pi}\left[\varrho - \frac{1}{2}\sin(2\varrho)\right] , \qquad (50)$$

where ϱ is the angle with vertex in the solar centre between the intersection of the solar disk edge with the horizon and the

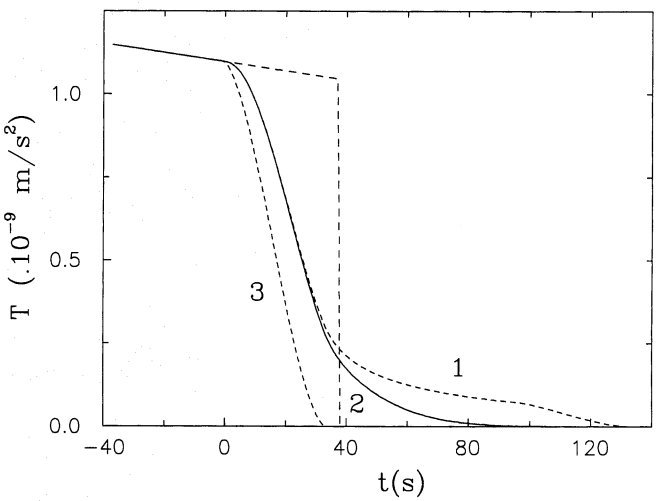

Fig. 10. Effects of introducing the correction accounting for the altitude decrease of the absorption coefficient. Curves 1, 2 and 3 correspond to the models without atmospheric absorption, with the $f_{\rm alt}$ correction factor introduced in Sect. 4.2.1, and with a constant absorption coefficient $\chi^\star$ corresponding to Rayleigh scattering at 550 nm, respectively. Normal atmospheric conditions have been assumed

top of the visible part of the disk. The results of this model for T are plotted in Fig. 9, together with the refractive penumbra decrease previously plotted in Fig. 6. As we already noted, the 'atmosphereless' penumbra decrease has a duration of 34 s, in exact agreement with the duration of the true penumbra phase in the more complicated, refractive model; however, the 'atmosphereless' model just results into a simple and structureless shape of the curve. The differences between the two curves can be physically interpreted in terms of the complex influence of atmospheric refraction, as explained earlier.

Let us now discuss the effects of the physical processes related to absorption on the penumbra perturbation curve. Figure 10 shows the importance of the correction factor which models the altitude decrease of the absorption coefficient, as discussed in Sect. 4.2.1: here the 'corrected' results (solid curve 2) are compared with the results obtained by neglecting absorption at all (curve 1) and with those coming from the simpler absorption model where the absorption coefficient is assumed to be constant throughout the atmosphere (curve 3). We observe that the latter model overestimates in a significant way the decrease of the perturbing force during phases I and II. Actually, apart from a nearly–constant time shift, curve 3 matches closely the 'atmosphereless' case of Fig. 9, and the constant–absorption case can be thought of as corresponding to an 'expanded' Earth, whose effective radius is somewhat increased by the existence of the atmospheric shell. As for the 'corrected' model yielding curve 2, in phase I its results are rather similar to those obtained without absorption, as the solar rays graze only the high

atmospheric layers having a low absorption coefficient. On the contrary, starting from the second part of phase II, when the solar disk is seen through the more absorptive bottom layers of the atmosphere, the corrected results become significantly lower than those of the absorption–free model, and actually are inter-

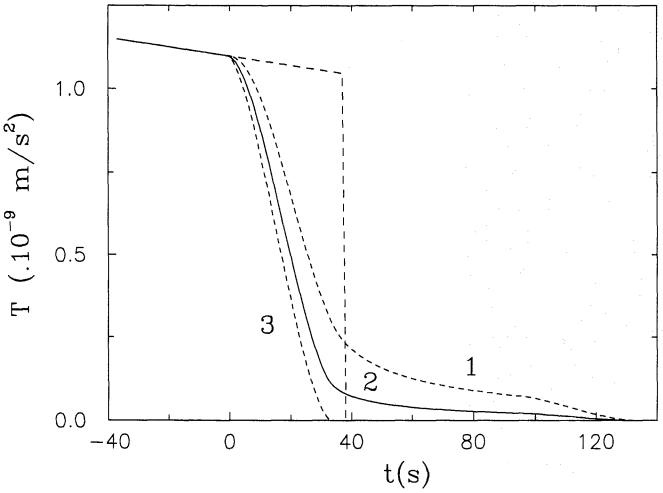

Fig. 11. Effects of introducing the correction accounting for the frequency–selective absorption in the atmosphere. Curves 1 and 3 are the same as in Fig. 10. Curve 2 corresponds to the model using the correction factor $f_{\rm red}$ derived in Sect. 4.2.2. Normal atmospheric conditions have been assumed

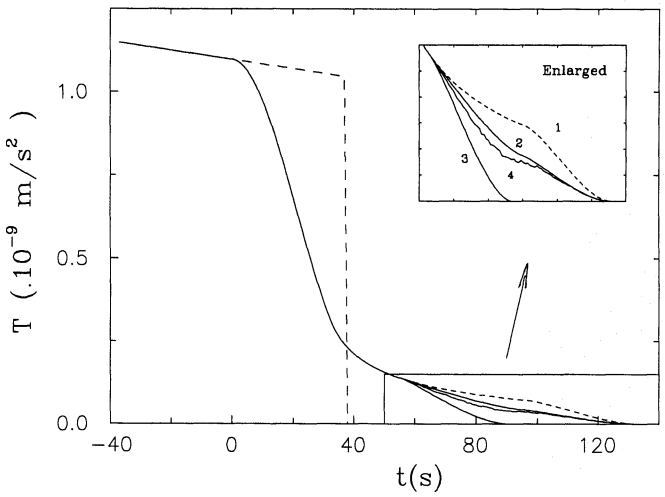

Fig. 12. Sensitivity of the penumbra decrease of T to the atmospheric conditions in the bottom 10–km thick layer. Curve 1 is the same as the no–absorption case of Fig. 6, whereas curves 2 and 3 have been derived assuming that the bottom layer has an absorption coefficient of 10^{-6} m^{-1} and 10^{-3} m^{-1}, respectively. Curve 4 results corresponds to a random choice of the absorption coefficient in the range between 0 and 10^{-3} m^{-1}, simulating a complex cloud coverage structure

mediate between those of the absorption–free and the constant–absorption models. This is consistent with the behaviour of the altitude correction factor, as discussed in Sect. 4.2.1.

Strong Rayleigh extinction for the Earth–grazing rays (i.e., those with zenith angles approaching 90°) is a well known and important effect in astronomy. Measurements are available (see e.g. Siedentopf & Scheffler 1965) up to zenith distances of about 87°. Extrapolating these data to the horizon we obtain a decrease of about 4 mag in the visual band. Taking into account that solar rays reaching the satellite cover in the atmosphere twice the distance as those seen by an Earth–surface observer, we estimate in about 8 mag the extinction decrease of intensity along an Earth–grazing ray. This corresponds to an attenuation factor of about 1600, in good agreement with the results of our computations, based on Eqs. (41) and (43). This factor is large enough to damp down the penumbra tail observed in Figs. 6 and 8.

In Fig. 11, we plotted again curves 1 and 3 from Fig. 10, and added the solid curve 2, which now represents the results obtained by taking into account a frequency–selective absorption through the factor $f_{\rm red}$ introduced in Sect. 4.2.2. Due to the overestimate of absorption at short wavelengths, mentioned in Sect. 4.2.2, the 'corrected' curve lies in between the two extreme models in which either no absorption or a frequency–independent absorption coefficient is assumed.

Figure 12 shows the possible effect of the presence of an optically dense bottom layer (due e.g. to cloud coverage): here curve 1 shows again the no–absorption results, while curves 2 and 3 correspond to a bottom atmospheric layer 10–km thick, having a constant absorption coefficient of 10^{-6} m^{-1} and 10^{-3} m^{-1}, respectively. Curve 4 shows the results of selecting at random for each (discrete) ray constituting the radiative flux and passing through the bottom 10–km of the atmosphere a value of the absorption coefficient in the range between 0 and 10^{-3} m^{-1}, in order to simulate a non–uniform cloud coverage. Note that as expected the penumbra tail is always depressed by absorption in the low atmosphere. In general, these results show that whereas atmospheric refraction generates a significant penumbra tail, the absorption processes tend to decrease its importance. Thus again we conclude that in reality the formation and extent of the tail depends sensitively on the atmospheric conditions prevailing over a very limited portion of the Earth's surface, about half a degree wide when seen from the satellite (some 100 km in size for LAGEOS). This may cause significant long–term residuals if the orbit is determined and/or predicted with dynamical models neglecting the complexities of the penumbra transition.

Finally, we will discuss the cases of satellites having orbits much higher or lower than that of LAGEOS. We sticked to the assumption of spherically symmetric satellites, though of course this does not apply to most real spacecraft, because in this paper we aim at illustrating the basic physics of the problem more than at producing realistic models for specific satellites. Figure 13 shows the T decrease curves during a penumbra transition for a hypothetical geostationary satellite, having a 42, 200 km orbital radius, such as the satellites tracked for geophysical purposes during the COGEOS campaign (Catalano et al. 1983; Nobili 1987). We have assumed typical values of the A/m and $\mathscr{C}_{\rm R}$ parameters (5×10^{-2} cm^2 g^{-1} and 1.5, respectively). Of course, other values of these parameters would just lead to rescale the vertical axis of the plot — whose horizontal axis still gives the time in seconds since the onset of the penumbra phenomena. The Sun has been assumed to lie on the Earth's equatorial plane, corresponding to an equinox date; note that for an equatorial satellite eclipses occur only when the solar latitude is less than about 9°, and that our choice implies that

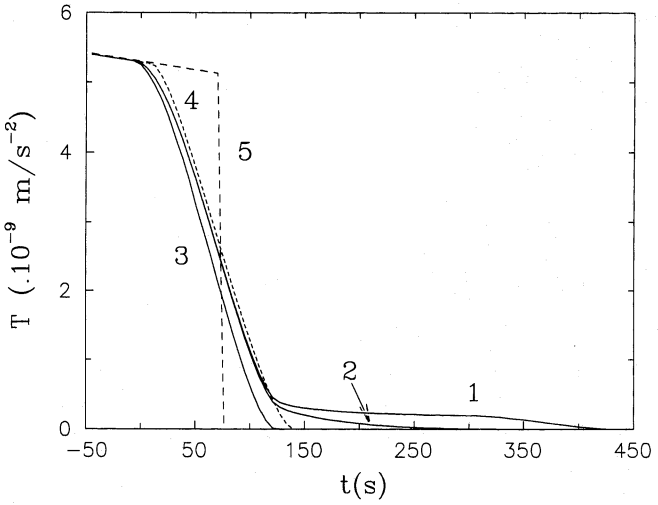

Fig. 13. T decrease curves during a penumbra transition for a hypothetical spherical geostationary satellite. The horizontal axis still gives the time in seconds starting from the beginning of the penumbra transition. Solid curves 1 and 3 have been obtained with the refraction–only and constant–absorption models, respectively; solid curve 2 corresponds to the altitude correction case; dashed curves 4 and 5 correspond to the simple 'atmosphereless Earth' and 'step approximation' models, respectively

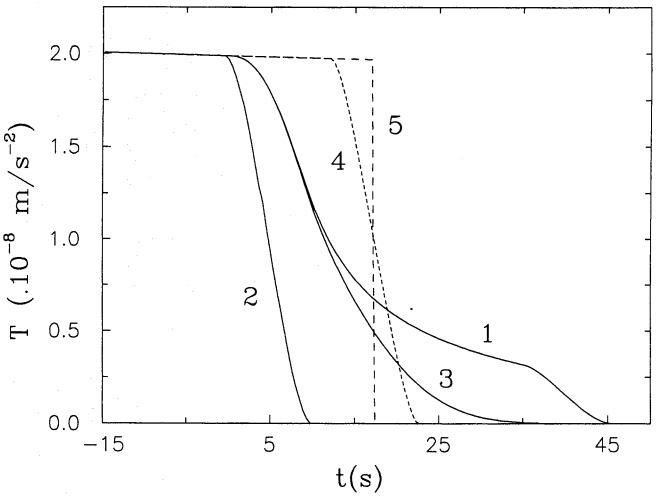

Fig. 14. The same as for Fig. 13, but for the (low) orbit planned for the MACEK accelerometric satellite

we are considering the shortest possible penumbra duration. The different curves correspond to the different models of the penumbra transition described earlier. Dashed curves 4 and 5 correspond to the simple 'atmosphereless Earth' and 'step approximation' models, respectively; solid curves 1 and 3 have been obtained with the models including refraction but no absorption and the constant absorption coefficient consistent with Rayleigh scattering, respectively; solid curve 2 corresponds to the more realistic altitude correction case. It is interesting to note that the no–absorption case (1) yields a very long tail, with the total penumbra transition spanning 428 s, but the value of T decreasing below 10% of the out–of–eclipse value in only about 120 s; in this case, at the end of phase II the vertical thickness of the solar 'disk' is only 0.75 arcmin! In case (2) the tail is reduced by absorption, but still lasts for some 100 s more than in the no–atmosphere case (4). The latter, however, is now a much better approximation than for LAGEOS: the reason of this is that the atmospheric layer, seen from the geostationary orbit, appears much thinner. Again, case (4) fairly resembles the constant–absorption case (3), apart from a short time lag.

Figure 14 has been derived for a satellite having the orbit planned for the MACEK microaccelerometric experiment (Peřestý & Sehnal 1992), i.e. a low orbit with perigee and apogee heights of 300 and 1300 km, respectively. The values of A/m and $\mathscr{C}_R$ are now 4×10^{-2} cm^2 g^{-1} and 1.2, respectively (note, however, that these values have a preliminary character, since the final configuration of the satellite has not been decided yet). The penumbra transition is assumed to occur near the apogee with the Sun's apparent trajectory normal to the local horizon, and again T is plotted vs. time starting from the entry into penumbra.

The five curves refer to the same models as for the geostationary satellite case. We can note that refraction effects are still important, but now the tail for curve 1 is much less extended than for higher orbits, and there is a more marked discontinuity at the end of phase II, owing to a smaller compression of the solar disk (minimum θ–thickness of 5.7 arcmin). The simple models yielding curves 3 and 4 still resemble each other, but are not good approximations of the more realistic case with altitude–dependent absorption coefficient (curve 2). The whole penumbra transition is of course shorter (46 s neglecting absorption and with normal atmospheric conditions), due to the higher orbital speed.

6. Conclusions

The main results obtained in this paper can be summarized as follows.

(1) We have presented a complete theory of the direct solar radiation pressure perturbations acting on artificial satellite orbits. The theory accounts for the occurrence of eclipses by the Earth, and in particular takes in detailed account the main physical processes which are at work during the passages through the Earth's penumbra. These complex processes have often subtle consequences, and the corresponding results display several non–intuitive features. The refraction phenomena — which have a crucial influence on the shape of the penumbra transition curve of the perturbing force — have been fully included in the theory, which is based on the assumption of a polytropic spherical atmosphere (Garfinkel 1967). On the other hand, several simplifying approximations have been made to take into account the atmospheric absorption and scattering processes.

(2) Possibly the least obvious effect of atmospheric refraction is the presence a fairly long–lived 'perturbation tail', occurring when the satellite would already be in the full shadow for an atmosphereless Earth. However, the magnitude and length

of this perturbation tail depend sensitively both on the orbit and on the physical conditions and the absorption properties of the atmosphere — hence e.g. on cloud coverage — over limited regions of the Earth's surface. For LAGEOS, this may cause significant long–term orbital residuals with respect to the predictions of simpler models for the penumbra radiation pressure perturbations. Concerning this, it is worth quoting here a remark by King–Hele in discussion following Baker (1970): '... The problem is the determination of the Earth shadow. If there happen to be clouds 10 km high at the point where the Sun's rays graze the horizon, the shadow height will be increased by over 10 km and, if the satellite is moving almost parallel to the shadow cone the position of the eclipse point can be altered by 100 km or more.' We will discuss in detail the possible consequences of such mechanisms related to peculiar orbit/shadow geometries in a forthcoming study (Vokrouhlický et al. 1993c).

(3) We aimed at producing a theory as realistic as possible, without caring much for its computational efficiency. As a consequence, the current numerical implementation of the theory is not suitable to analyze orbital arcs longer than a few revolutions, due to the great CPU time demands associated with the short time step and the complex calculation to be carried out during the penumbra transitions. On the other hand, approximate formulations are under study which will hopefully allow us to apply the penumbra theory to specific open problems in satellite dynamics, such as the interpretation of LAGEOS' observed residuals (Vokrouhlický et al. 1993c) and the analysis of non–gravitational perturbations undergone by satellites equipped with accurate accelerometers (e.g., the CACTUS mission carried out in the 80s and the planned MACEK mission). This is a delicate task, because the physical mechanisms at work during the penumbra transition are complex and their outcome may depend on the specific atmospheric conditions.

(4) For the sake of simplicity, we have applied our theory to a spherical LAGEOS–like satellite. However, the main body of the theory, including the treatment of the penumbra phase processes, is independent of the spherical symmetry assumption. Once the radiative field at the satellite's position is known, one can always use formulae generalizing (11) and (22) to compute the radiative force in the case of a general satellite shape (see Vokrouhlický & Sehnal 1993b; Vokrouhlický et al. 1993a).

Acknowledgements. The authors thank Dr. V. de Moraes for several suggestions improving the first version of the paper. This work was completed while one of the authors (P.F.) was staying at the Observatoire de la Côte d'Azur (Dept. Cassini, Nice) thanks to the 'G. Colombo' fellowship of the European Space Agency. D.V. is grateful to the Observatoire de la Côte d'Azur (Dept. CERGA, Grasse) for kind hospitality. Partial support by the Italian Space Agency (ASI) is also acknowledged.

References

Aksenov E.P., 1977, Theory of Motion of Artificial Satellites of the Earth, Nauka, Moscow, 1977 (in Russian)
Aksnes K., 1976, Celest. Mech. 13, 89
Allen C.W., 1976, Astrophysical Quantities, Athlone Press, London
Anselmo L., Bertotti B., Farinella P., Milani A., Nobili A.M., 1983, Celest. Mech. 29, 27
Baker R.M.L., 1970, Radiation on a satellite in the presence of partly diffuse and partly specular reflecting body, In: J. Kovalevsky (ed.) Trajectories of artificial celestial bodies. Springer–Verlag, Berlin, p. 85
Barlier F., Carpino M., Farinella P., et al., 1986, Ann. Geophys. 4, 193
Brookes C.J., Ryland F.C.E., 1982a, Celest. Mech. 27, 339
Brookes C.J., Ryland F.C.E., 1982b, Celest. Mech. 27, 353
Brouwer D., Clemence G., 1961, Methods of Celestial Mechanics, Academic Press, New York/London
Catalano S., McCrosky R., Milani A., Nobili A.M., 1983, J. Geophys. Res. 88, 669
Chandrasekhar S., 1950, Radiative Transfer, Oxford Univ. Press, Oxford
Ferraz–Mello S., 1964, C.R. Acad. Sci. Paris 258, 463
Ferraz–Mello S., 1972, Celest. Mech. 5, 80
Fesenkov W.G., 1967, AZh 44, 3
Garfinkel B., 1944, AJ 50, 169
Garfinkel B., 1967, AJ 72, 235
Van de Hulst H.C., 1980, Multiple Light Scattering (Tables, Formulas, and Applications), Academic Press, New York
Kabeláč J., 1988, Bull. Astron. Inst. Czech. 39, 213
Kozai Y., 1961, Effects of solar radiation pressure on the motion of an artificial satellite, SAO Spec. Report 56
Lála P., 1971, Bull. Astron. Inst. Czech. 22, 63
Lála P., Sehnal L., 1969, Bull. Astron. Inst. Czech. 20, 327
Liou K.-N., 1980, An introduction to Atmospheric Radiation, Academic Press, New York
Link F., 1933, Bull. Astron. 8, 77
Link F., 1962, Bull. Astron. Inst. Czech. 13, 1
Link F., 1969, Eclipse Phenomena in Astronomy, Springer–Verlag, Berlin
Link F., Neužil L., 1969, Tables of Light Trajectories in the Terrestrial Atmosphere, Hermann, Paris
McCartney E.J., 1976, Optics of the Atmosphere (Scattering by Molecules and Particles), J. Willey & Sons, New York
Mihalas D., 1970, Stellar Atmospheres, W.H. Freeman and Co., San Francisco
Milani A., Nobili A.M., Farinella P., 1987, Non–Gravitational Perturbations and Satellite Geodesy, A. Hilger, Bristol
Moore P., 1979, Celest. Mech. 20, 125
Musen P., 1960, J. Geophys. Res. 65, 1391
Musen P., Bryant R., Bailie A., 1960, Sci 131, 935
Murray C.A., 1983, Vectorial Astrometry, A. Hilger, Bristol
Nobili A.M., 1987, CSTG Bulletin 9, 19
Parkinson R.W., Jones H.M., Shapiro I.I., 1960, Sci 131, 920
Pérez-Jordá J.M., San-Fabián E., Moscardó F., 1992, Comp. Phys. Communicat. 70, 271
Peřestý R., Sehnal L., 1992, In–orbit microaccerelerometric experiment, presented at the 43rd congress of the International Astronautical Federation, Washington DC
Polyakhova E.N., 1963, Bull. Inst. Theor. Astron. 13, 15 (in Russian)
Rigaud P., 1967, C.R. Acad. Sci. Paris 265, 1504
Rubincam D.P., Weiss N.R., 1986, Celest. Mech. 38, 233
Sampson R., 1993, Sky & Telescope (February), 96
Scharroo R., Wakker K.F., Ambrosius B.A.C., Noomen R., 1991, J. Geophys. Res. 96, 729
Shapiro I.I., Jones H.M., 1960, Sci 132, 1484

Siedentopf H., Scheffler, 1965, Astronomical instruments: Influence of the Earth's atmosphere, In: Voigt H.H. (ed.) Landolt-Börnstein numerical data and functional relationships in science and technology. Springer–Verlag, Berlin, p. 48

Slowey J.W., 1974, Radiation-pressure and air-drag effects on the orbit of the balloon satellite 1963 30D, SAO Spec. Report 356

Smith D.E., Dunn P.J., 1980, Geophys. Res. Lett. 7, 437

Sobolev V.V., 1975, Light Scattering in Planetary Atmospheres, Pergamon Press, Oxford

Vashkovyak S.N., 1976, AZh 53, 1085 (in Russian)

Vokrouhlický D., Sehnal L., 1993a, Celest. Mech. 56, 471.

Vokrouhlický D., Sehnal L., 1993b, Celest. Mech., in press

Vokrouhlický D., Farinella P., Lucchesi D., 1993a, Celest. Mech., in press

Vokrouhlický D., Farinella P., Lucchesi D., 1993b, A&A, in press

Vokrouhlický D., Farinella P., Mignard F., 1993c, in preparation

Wyatt S.P., 1961, The effect of radiation pressure on the secular acceleration of satellites, SAO Spec. Report 60

Zadunaisky P.E, Shapiro I.I., Jones H.M., 1961, Experimental and theoretical results on the orbit of ECHO I, SAO Spec. Report 61

Zerbini S., 1980, Celest. Mech. 22, 307

This article was processed by the author using Springer-Verlag TEX A&A macro package 1992.